2014

Ultra-small fluorescent inorganic nanoparticles for bioimaging

Zhen Li
University of Wollongong, zhenl@uow.edu.au

Qiao Sun
University of Queensland

Yian Zhu
University of Queensland

Bien Tan
Huazhong University of Science and Technology

Zhi Ping Xu
University of Queensland

See next page for additional authors

Ultra-small fluorescent inorganic nanoparticles for bioimaging

Abstract
The novel optical, electrical, and magnetic properties of ultra-small inorganic nanoparticles make them very attractive in diverse applications in the fields of health, clean and renewable energy, and environmental sustainability. This article comprehensively summarizes state-of-the-art fluorescence imaging using ultra-small nanoparticles as probes, including quantum dots, metal nanoclusters, carbon nanomaterials, up-conversion, and silicon nanomaterials.

Keywords
inorganic, nanoparticles, bioimaging, fluorescent, small, ultra

Disciplines
Engineering | Physical Sciences and Mathematics

Authors
Zhen Li, Qiao Sun, Yian Zhu, Bien Tan, Zhi Ping Xu, and S X. Dou

Ultra-small fluorescent inorganic nanoparticles for bioimaging

Zhen Li,*[a] Qiao Sun,[b] Yian Zhu,[b] Bien Tan,[c] Zhi Ping Xu,*[b] and Shi Xue Dou[a]

The novel optical, electrical, and magnetic properties of ultra-small inorganic nanoparticles make them very attractive in diverse applications in the fields of health, clean and renewable energy, and environmental sustainability. This article comprehensively summarizes state-of-the-art fluorescence imaging using ultra-small nanoparticles as probes, including quantum dots, metal nanoclusters, carbon nanomaterials, up-conversion, and silicon nanomaterials.

1 Introduction

When the size of inorganic materials is reduced to the nanoscale range, they exhibit unusual optical, electrical, magnetic, mechanical, and chemical properties, distinctly different from those in their bulk analogues. For example, semiconductor nanocrystals (usually referred to as quantum dots (QDs)) exhibit strong size-dependence of their optical properties when their size is smaller than the Bohr exciton radius.[1] Magnetic iron oxide nanoparticles become superparamagnetic when their size is reduced below the critical size where they behave as individual magnetic domains.[2] Carbon nanotubes show remarkable tensile strength,[3] and graphene exhibits remarkably high electron mobility.[4] Their novel properties make these nanomaterials very attractive in diverse applications, ranging from energy conversion and storage to biomedical imaging. In this article, we summarize the recent advances in ultra-small inorganic nanoparticles for fluorescence imaging (Table 1), especially those smaller than 10 nm as they are easily taken up and excreted, and show longer blood circulation time in comparison with larger ones.

For fluorescent materials, there are two kinds of photoluminescence mechanisms, i.e. down conversion and up conversion.[5] The down-conversion process normally absorbs one high energy photon and emits a low energy photon, e.g. a Stokes-shift emission. In contrast, up-conversion is an anti-Stokes process that converts the absorbed low energy light into higher energy emission via multiple absorptions or energy transfer processes. The fluorescence generated by both processes has long been used in molecular imaging to visualize cell biology at many levels.[6, 7] The first fluorescence imaging could be dated back to 1924 when Policard observed red fluorescence from endogenous porphyrins in tumours illuminated with an ultraviolet light.[8] Since then, advances in molecular biology, organic chemistry and material science have revealed several classes of promising probes for fluorescence imaging, which include small organic dyes, fluorescent proteins, and fluorescent inorganic nanoparticles.[6] Compared with organic dyes and fluorescent proteins, fluorescent inorganic nanoparticles have several distinct advantages. For example, QDs have high absorbance, high QY, narrow emission, large Stokes shifts, and high resistance to photobleaching.[9] These properties render them robust for fluorescent probes for biolabelling and bioimaging.[9-12] In recent years, other fluorescent nanomaterials, such as ultra-small metal nanoclusters, fluorescent carbon and graphene dots, up-conversion nanocrystals, and silicon nanoparticles have been exploited as alternatives to conventional QDs. In the following sections, we introduce these fluorescent nanomaterials from viewpoints of preparation and functionalization to satisfy the requirements for routine labelling and imaging of cells and tissues. Advanced applications of fluorescent nanomaterials in living systems as sensors for enzyme, oxygen, metal ions, and pH, have readily been described elsewhere.[13-16]

For bioimaging, fluorescent nanoparticles should have water-solubility, biocompatibility, chemical- and photo-stability. They should also have uniform size and high quantum yield (QY) for optimized brightness, narrow and symmetric emission for multiplexing and colour saturation, and minimized blinking for light output stability. In the second part, we introduce the development in synthesis and surface modification of fluorescent QDs (especially CdSe- and CdTe based II-VI QDs) to result in water-soluble, biocompatible and highly stable QDs with high QY, together with their routine bioimaging applications and their toxicity. In the third section, we describe extremely small metal nanoclusters (usually smaller than 2 nm) as an emerging fluorescent probes, and address the difficulties in their synthesis, characterization, modification, and imaging application. In the fourth part, we bring in carbon-based fluorescent nanoprobes including carbon dots and graphene quantum dots (GQDs), which are usually smaller than 10 nm. These carbon-based nanoprobes have excellent biocompatibility and unique properties (e.g. both up-conversion and down-conversion emissions). In the fifth section, we briefly introduce lanthanide-based up-conversion nanocrystals, which have attracted considerable attention in recent years. Most of up-conversion nanoprobes have a large size (>10 nm) and are out of the scope of this article. In the sixth part, we discuss fluorescent silicon nanoparticles, which have excellent biocompatibility and stability. In the last part, we highlight the major challenges and perspectives of ultra-small fluorescent

nanoparticles and fluorescence bioimaging.

Table 1. Comparison of different types of fluorescent inorganic nanoparticles.

Types	Representatives	Preparation	Size (nm)	Advantages	Disadvantages	Applications
QDs	CdSe, CdTe, InP, CuInS$_2$, CuInSe$_2$, and their core-shell nanostructures	Solvothermal and hydrothermal methods	< 10	Tuneable size and fluorescence, high QY and relatively stable	toxicity	Fluorescent labels and sensors
Metal NCs	Au, Ag, Cu, Pt, Pd	Reduction of metal salts or etching of large metal nanoparticles	< 2	Ultra-small size, easily taken up and excreted.	sensitive fluorescence, difficult for modification and functionalization	Imaging of cells and tissues. Sensors
Carbon-based materials	C-dots, GQDs	Solvothermal and hydrothermal methods	<10	Tunable fluorescence, excellent biocompatibility	Instability and unclear of fluorescence mechanism	Fluorescent biomarkers and sensors
UCNs	Yb^{3+}/Ln^{3+}-doped NaYF$_4$, GdYF$_4$, and their core-shell nanostructures	Solvothermal and hydrothermal methods	most >10, few <10	low background, large anti-Stokes shifts, sharp emission, high stability, deep penetration	Low QY, potential toxicity	Multimodal imaging agents and drug carriers
Si NPs	Si	Etching annealed SiO$_x$, reduction of SiCl$_4$, and reaction of Na$_4$Si$_4$ with NH$_4$Br	< 5	Small size, Ultrahigh stability	Laborious synthesis, Low QY, Difficult to tune fluorescence	Long-term imaging and labeling

QDs: quantum dots; UCNs: up-conversion nanocrystals; NPs: nanoparticles; GQDs: graphene quantum dots; QY: quantum yield

2 Semiconducting Fluorescent QDs

2.1 Synthesis of monodisperse QDs with high QYs

Fluorescent QDs include semiconducting nanoparticles from Groups IV (Si and Ge dots),[17-20] II-VI (CdE and ZnE, E = S, Se, and Te), III-V (InP), and I-III-VI (CuInS$_2$, CuInSe$_2$),[21-23] in which the II-VI QDs (especially CdSe and CdTe based QDs) have been extensively investigated as prototypes of semiconductor QDs due to their strong quantum confinement effects and high fluorescence QYs. II-VI colloidal fluorescent QDs can be prepared in organic solvents or aqueous solutions. Organic routes are usually selected to prepare monodisperse and highly fluorescent QDs. Discovered in 1981, QDs did not receive intensive attention until 1993, when a breakthrough in preparation of colloidal QDs in solution was achieved.[24] Monodisperse cadmium chalcogenide (CdE, E = S, Se, and/or Te) QDs were prepared by fast injection of a solution of precursors (organometallic Cd and Se/S/Te dissolved in trioctylphosphine (TOP)) into a high-boiling-point (~ 300 °C) coordinating solvent trioctylphosphine oxide (TOPO).[24] These QDs had a narrow particle size distribution with 10% standard deviation, which was reduced to 5% after size-selective precipitation. Their fluorescent QY was about 10%.

The key in this "TOPO-TOP" approach is a burst of nucleation which can be effectively separated from the growth process.[25] The use of highly flammable and toxic dimethylcadmium, however, limited the applicability of this approach at that time. Extensive efforts have been made to develop and optimize this approach by using various stable and low toxicity precursors[26] (e.g. cadmium oxide, CdO;

cadmium carboxylate, Cd(OOCR)$_2$; selenium oxide, SeO$_2$, etc.), non-coordinating solvents (e.g. 1-octadecene, ODE) and stabilizers[27] (e.g. octyldiphenylamine (ODPA), diethylenetriaminepentaacetic acid (DTPA), hexadecyl amine (HDA), etc.) to generate monodisperse QDs with high QY.

Monodisperse II-VI QDs with different sizes and shapes can be obtained by controlling their nucleation and growth processes through optimization of monomer concentration and reactivity, molar ratio, reaction temperature, ligands, etc. (Figure 1).[28-31] It has been found that slight modification of reaction parameters can lead to a broad variety of particle sizes and shapes. For example, Peng *et al.* demonstrated that the size and size distribution of CdSe dots can be manipulated by the monomer concentration.[32] At high monomer concentrations, the smaller nanoparticles grow faster than larger ones, which results in the size distribution being "focused". If the monomer concentration drops below a critical threshold, the smaller particles are depleted as larger ones grow (i.e. Ostwald ripening), and the size distribution gets broader or is "defocused". Controlling the nanoparticle growth kinetics can result in a narrow particle size distribution (5% standard deviation) without the size-selective precipitation.[32]

It was observed that the QY increased monotonically to the maximum value and then decreased with the growth time.[33] Such a photoluminescence bright point indicates an optimal surface structure/reconstruction. Use of a large Se/Cd ratio (10/1) can result in very bright CdSe QDs with QY of 85% at room temperature. The high QY of these QDs is attributed to stabilization of organic ligands on the surface. Since these ligands can be chemically degraded and detached from the surface, the photo- and chemical stability of the core is
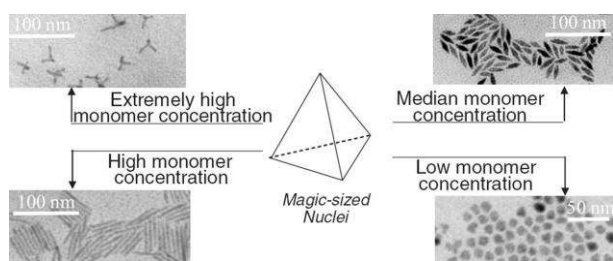
Figure 1. Transmission electron microscope (TEM) images and growth paths of CdSe nanocrystals with different morphology. Reproduced from Ref. 30.
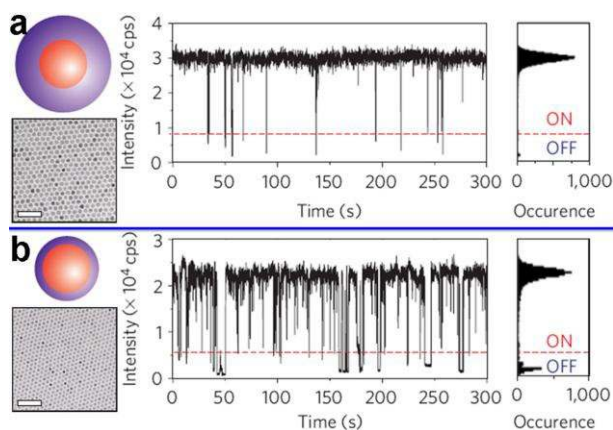

Figure 2. TEM images and blinking behaviour of core-shell CdSe@CdS nanoparticles: (a) 2.2 nm CdSe core with 2.4 nm CdS shell; (b) 2.2 nm CdSe core with 0.7 nm CdS shell. Reproduced from Ref. 36.

sometimes severely affected. In order to improve their luminescence and photostability, wide-band-gap shells (e.g. cadmium sulphide (CdS) and zinc sulphide (ZnS)) have been coated onto their surface to form core-shell QDs.[34, 35] Li *et al.* developed a successive ion layer adsorption and reaction (SILAR) technique to epitaxially grow shells in a non-coordinating solvent.[34] The resultant core-shell CdSe@CdS QDs had a QY of 40%. Xie and his co-workers further developed this approach to prepare CdSe-core-multishell QDs with QY up to 85%.[35] Recently, Chen *et al.* used cadmium oleate and octanethiol as Cd- and S-precursors, and prepared nearly perfect core-shell CdSe@CdS QDs with the highest QY (97%) ever reported (Figure 2).[36] The slow continuous precursor infusion and the relatively low reactivity of octanethiol provide optimal conditions for passivation of the CdSe surface and growth of the CdS shell. Compared with conventional core-shell CdSe@CdS QDs, these new QDs featured significantly suppressed blinking, with an average fluorescence on/off time ratio of 94:6 for single large core-shell nanocrystals (Figure 2). The blinking was gradually suppressed with increasing shell thickness.[36] In addition to Wurtzite core-shell CdSe@CdS QDs, zinc-blende core-shell analogues with suppressed blinking (>95% on time) were also prepared by Qin and co-workers.[37] These zinc blende core-shell CdSe@CdS QDs exhibited a QY of 90%. It should be noted that non-blinking core-shell CdZnSe@ZnSe QDs, which exhibited complete suppression of blinking on the time scale from milliseconds to hours, were successfully prepared

by Wang *et al.*[38] The high fluorescence QY and non-blinking QDs make them very useful in applications requiring a continuous output of single photons.

During the preparation of QDs, attempts to adjust the growth kinetics of the QDs incidentally led to the development of one-dimensional (1D) nanorods.[29] By using very high precursor concentrations and a defined admixture of alkylphosphonic acids and trioctylphosphine oxide (TOPO), 1D and even more complex structures such as arrows, teardrops, or tetrapods were synthesized (Figure 1).[30] Recently, we demonstrated that doped and undoped 1D semiconductor nanostructures can be produced by using a lower precursor concentration in the presence of bismuth nanoparticles.[39-44] This is in contrast to the synthesis of 1D nanostructures without nanocatalysts. These nanowires exhibited unusual optical,[45, 46] electronic,[47, 48] and magnetic[40] properties with potential diverse applications.[48, 49] The fast growth process resulted in crystal twinning and defects in the nanowires,[50, 51] leading to a low fluorescence QY (< 1%) which could be improved by more than three times through coating with a wide-band-gap shell.[52]

Despite monodispersity, high QY, and stability, these QDs generated in organic solvents are normally hydrophobic and have to be modified in order to be water-soluble and biocompatible for bioapplications. The modification leads to the decrease in fluorescence QY, e.g. the QY of above perfect core-shell CdSe@CdS QDs decreased from 94% to 77% after transferred into PBS solution with PEG-SH.[36] Therefore, direct preparation of QDs in aqueous solution has been developed almost simultaneously.

The aqueous approach was firstly adopted by Henglein *et al.* to prepare CdS nanoclusters in 1982.[53] They also reported the first example of the preparation of CdTe QDs in aqueous solution.[54] The resultant CdTe QDs did not show fluorescence, however. Rogach *et al.* synthesized stable fluorescent CdTe QDs with a QY of 3% by using thioglycerol and mercaptoethanol as stabilizers.[55] Later on, many efforts were made to improve QD fluorescence QY by using different stabilizers (thioglycolic acid (TGA); mercaptopropionic acid (MPA)), precursor ratios, and manners of heating (hydrothermal and microwave methods).[56] Under the optimal conditions, the QY of water-soluble CdTe-based QDs can reach as high as 84%, which is comparable to that of the above-mentioned hydrophobic QDs. High fluorescence QY also can be obtained by surface modification of as-synthesized QDs with illumination. For example, the fluorescence QY of CdTe QDs was drastically improved from 8% to 85% after 28-day illumination, due to the formation of the core-shell structure (i.e. CdTe@CdS) with the assistance of illumination.[57]

The above water-soluble QDs were normally prepared in strong basic solution (pH > 8), which limits their bio-applications, as most biological activities take place under neutral-pH conditions. Adjusting the solution pH to neutral could quench the fluorescence of the QDs. Therefore, it is of great interest to develop a novel approach for preparing highly fluorescent water-soluble QDs from stable precursors under neutral pH conditions. Recently, we have successfully synthesized highly fluorescent (84% QY) mercaptosuccinic acid

Figure 3. Tunable core-shell CdTe@CdS QDs with high stability. Reproduced from Ref. 58.

(MSA)-capped CdTe/CdS QDs using stable Na_2TeO_3 as the Te source via a one-pot reaction under neutral conditions (Figure 3).[58] A novelty of this approach is the use of MSA, which exhibits the features (pK_{COOH1} = 3.30, and pK_{COOH2} = 4.94) of both TGA (pK_{COOH} = 3.53) and MPA (pK_{COOH} = 4.32) in terms of acidity. MSA can effectively stabilize QDs in a wider pH range (pH = 6 – 9) with better protection because of its stronger interactions with the surface Cd^{2+} ions and its stronger steric effects. In addition, slow decomposition of MSA-Cd complexes forms a thin layer of CdS on the surface of CdTe nanocrystals, decreasing the surface defects and leading to high fluorescence QY. Another novelty is the use of sodium citrate as buffer. The resultant QDs show higher fluorescence QY than those stabilized with TGA or MPA obtained from the conventional aqueous method. They also show lower cytotoxicity at certain concentrations due to the unique structure of MSA and the formation of a CdS shell on the surface of the CdTe core.[58]

In addition to organic and aqueous routes, QDs can be produced in living organisms. Stürzenbaum *et al.* demonstrated that the earthworm's metal detoxification pathway can be exploited to produce water-soluble and biocompatible CdTe QDs.[59] This bioapproach is time-consuming (11 days), however, and the resultant QDs have a low fluorescence QY (8%), so this method cannot be used for large-scale preparation.

2.2 Surface modification of QDs

From the viewpoint of bioapplications, QDs should have excellent water-solubility, biocompatibility, and stability. These properties not only depend on their particle size, shape and composition, but also rely on their surface structure and surface charge. More importantly, the surface properties of QDs determine their bio-interface interactions, cellular endocytosis and intracellular distribution, *in vivo* biodistributions, metabolism, and fate.[60-63] Engineering surface of QDs therefore becomes highly important as this process can improve these properties and introduce additional functions.[10] Medintz *et al.* recently summarized the strategies for surface modification and bioconjugation of QDs.[11] One popular strategy for hydrophobic QDs is ligand exchange, which not only transfers them from organic solvents into aqueous solution, but also provides functional groups for further conjugation with biomolecules.[64] Small water-soluble molecules such as TGA, MPA, and
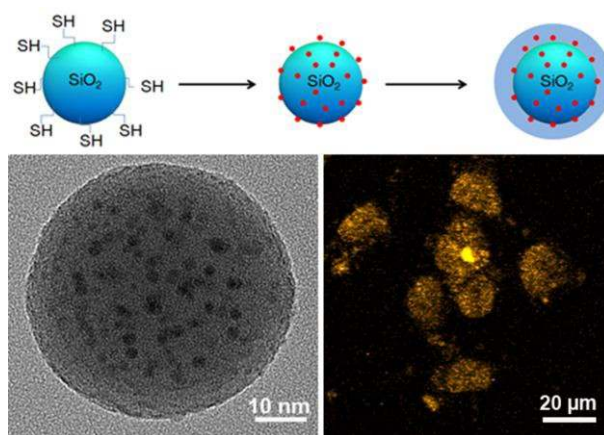

Figure 4. Preparation of sandwich-like SiO_2@CdTe@SiO_2 nanoparticles for cell labeling. Reproduced from Ref. 72.

dihydrolipoic acid (DHLA) are often used. Unfortunately, ligand-exchange can lead to a huge loss of fluorescence due to the changes in surface properties. These small molecules cannot prevent QDs from oxidation and degradation. Thereby a number of polymers (e.g. polyethylene glycol (PEG), and polyethylenimine (PEI)), proteins, peptides, and liposomes have been adopted to coat QDs.[12] Similar to small-molecule modified QDs, these surface-coated flexible polymers and biomolecules are less resistant to oxygen and chemicals, and have little impact on the improvement of the photo- and chemical stability of QDs. Therefore, organic-modified QDs still face the issues of toxicity, instability and the loss of fluorescence, despite the significant progress achieved in recent years.

Compared with unmodified and organically modified QDs, QDs coated with an inorganic shell show higher stability in terms of both chemistry and fluorescence. Silica is one of the most popular inert materials used for surface modification, and has a few distinct advantages,[65] including: (1) a non-porous silica shell can protect QDs from environmental damage and improve their stability;[66] (2) the silica shell can effectively inhibit the release of toxic Cd^{2+} ions and thus reduce the QDs' toxicity;[66] (3) the silica coating can provide a hydrophilic surface and functional groups for conjugating with biomolecules.[67] The silica shell can be formed on the surface of the QDs by the Stöber method[68] or the reverse microemulsion approach.[69] Both methods have their own advantages and disadvantages, but one common challenge is the preparation of highly fluorescent QDs@SiO_2 nanoparticles with tuneable size, as the fluorescence of QDs is drastically decreased during silica coating.

In 2004, Nann *et al.* prepared single-dot@SiO_2 nanoparticles by the Stöber method.[70] Yang and his co-workers prepared similar CdTe@SiO_2 nanoparticles by the reverse microemulsion approach.[69] These single-dot@SiO_2 nanoparticles show a low fluorescence QY (< 10%), however. Later on, the fluorescence QY of CdTe@SiO_2 nanoparticles was improved to 47%. In comparison with incubated CdTe QDs (83%), nearly 40% of the fluorescence was still lost during silica coating.[71] The formation of single-dot@SiO_2 nanoparticles is attributed to the electrostatic repulsion between QDs and silica intermediates.

In order to improve the fluorescence QY and the number of QDs in each SiO_2 nanoparticle, we successfully prepared sandwich-like SiO_2@CdTe@SiO_2 (SQS) nanoparticles using a
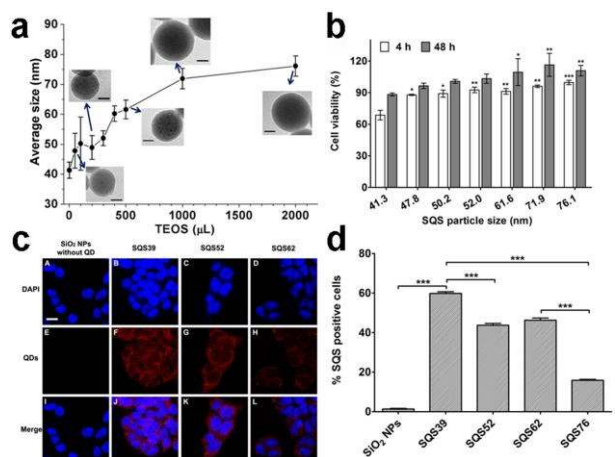
Figure 5. (a) Size-dependence of SiO$_2$@CdTe@SiO$_2$ nanoparticles on tetraethyl orthosilicate (TEOS) volume; **(b-d)** size-dependence of cytotoxicity and cell uptake. Reproduced from Ref. 74.

Figure 6. (a) Structure of a multifunctional QD probe; **(b)** C4-2 cells labelled with multifunctional QDs; **(c)** *In vivo* targeted imaging using multifunctional QDs; **(d)** multicolour capability of QD imaging in live mouse. Reproduced from Ref. 76.

novel strategy (Figure 4).[72] We started from the synthesis of the thiol-capped SiO$_2$ core. The surface thiol groups can tightly anchor CdTe QDs on the surface of SiO$_2$ nanospheres. Then, a silica layer was coated on the SiO$_2$@CdTe to form SQS nanoparticles. During the silica coating, it is important to add an appropriate amount of 3-mercaptopropyl-trimethoxysilane (MPS) for pre-coating in order to get highly fluorescent sandwich-like nanoparticles. Compared with other QDs@SiO$_2$ nanoparticles, our SQS nanopaticles show the highest fluorescence QY ever reported (up to 61%). They also show higher stability and lower toxicity in comparison with SiO$_2$@CdTe nanoparticles.

During the modification of QDs, the overall particle size has to be strictly controlled because it can dramatically influence the nanoparticle biological behaviour, such as cell internalization, tumour targeting and penetration, *in vivo* systemic and lymphatic biodistribution, metabolism, and clearance. Nanoparticles with a size of 20-60 nm have shown distinct biodistribution, tumour penetration, and cellular tracking properties.[73] Therefore, we prepared a series of SQS nanopaticles with sizes in the range of 39 nm to 76 nm by controlling the reaction parameters, including the amount and the type of silica precursor, the ratio of silica precursor to ammonia, and the ratio of H$_2$O to surfactant.[74] These SQS nanoparticles exhibited strong size dependence of their stability, toxicity, and cellular uptake (Figure 5). Our findings highlight the importance of controlling particle size and shell thickness during the preparation of fluorescent QDs@SiO$_2$ core-shell nanoparticles.

2.3 Fluorescence imaging of QDs

The earliest bioapplications of fluorescent QDs were reported in 1998.[64, 67] Bruchez *et al.* coated core-shell CdSe@CdS QDs with a thin layer of silica and then conjugated them with biotin.[67] The biotinylated QDs were successfully applied to label 3T3 mouse fibroblast cells. Chan *et al.* used small molecule TGA to transfer hydrophobic CdSe@ZnS QDs into water solution, and then conjugated them with transferrin proteins.[64] The authors incubated TGA-modified QDs and transferrin-QD conjugates with HeLa cells, respectively, and found that no QDs could be observed inside the cell in the absence of transferrin. In contrast,
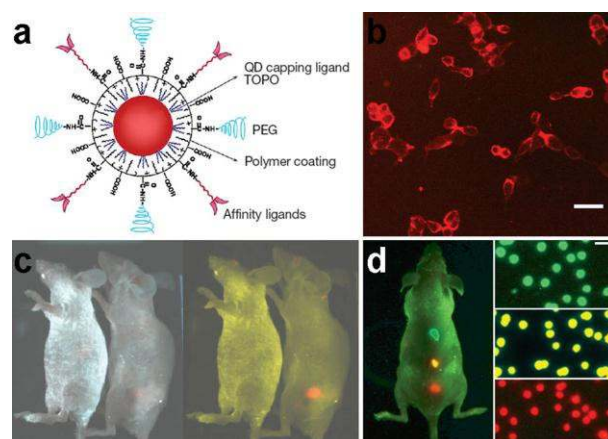
QDs were internalized into the cells in the presence of transferrin due to the occurrence of receptor-mediated endocytosis.

Motivated by the above pioneering research, extensive nonspecific and targeted bio-labelling and imaging have been carried out at different levels, ranging from *in vitro* to *in vivo* models.[10-12] Nonspecific cellular labelling involves the use of hydrophobic and electrostatic interactions between surface-capping molecules of QDs and biomolecules in the cell membrane. Thus, their surface ligand properties and the cell type largely determine the nonspecific adsorption and uptake of QDs. In most cases, such nonspecific adsorption is unwanted, as this reduces the selectivity and targeting efficiency. In order to overcome nonspecific adsorption, PEG and its derivatives have been used to modify the QD surface, as they can effectively minimize and prevent the nonspecific interactions of QDs with biomolecules, cells, and tissues.

Similar to the *in vitro* nonspecific adsorption of cells, non-targeted QDs can accumulate within tumours through the enhanced permeability and retention (EPR) effect. Such passive targeting is attributed to the leakiness of the tumour vasculature and the poor lymphatic drainage, which enables QDs or other nanoparticles to accumulate in tumours.[75] The EPR effect could lead to more than 50 times as great nanoparticle accumulation in tumours compared with healthy tissues. It is difficult, however, to maximize nanoparticle accumulation through the EPR effect, as this effect varies from tumour to tumour, and strongly depends on the particle size and the surface charge.[75] In addition, the EPR effect is not commonly observed in some types of cancers such as gastric and pancreatic cancers.

An alternative approach is active targeting, which can be achieved by conjugating QDs with targeting moieties such as small molecules (e.g. folic acid and hyaluronic acid), peptides (e.g. arginine-glycine-aspartic acid (RGD)), and proteins (e.g. antibodies, antibody fragments, transferrin, etc.).[12] In 2004, Gao and colleagues reported a landmark work on *in vivo* cancer targeting with QDs (Figure 6).[76] They first encapsulated hydrophobic CdSe@ZnS core-shell QDs with an ABC triblock copolymer (i.e. polybutylacrylate-polyethylacrylate-polymethacrylic acid) by using hydrophobic-hydrophobic

interactions between the capping ligands of QDs and the hydrophobic segments of the block copolymer. Then, they conjugated tumour-targeting ligands and drug-delivery functionalities with the polymethacrylic acid segment. The *in vivo* study showed that these QD probes accumulated at the tumour site through the EPR effect, and the specific antibody-antigen interactions. It is worth mentioning that passive targeting is much slower and less efficient than active targeting.

Although targeted nanoparticles hold much promise, and the concept was introduced more than 30 years ago, none of them has been clinically approved.[75] One possible reason is the huge gap between cost and benefit. Compared with expensive antibodies and other targeting ligands, cost-effective small molecules such as folic acid have been adopted. Folic acid and folate conjugates can be specifically recognized by the folate receptor (FR), which is a glycosylphosphatidylinositol-anchored protein. The alpha isoform of FR (FR-α) is found to be overexpressed in many epithelial cancers, but not highly expressed in normal tissues except for the kidney. Since the affinity of FR to folic acid and folate conjugates is relatively high ($K_d \approx 100$ pM), FR-α has been extensively investigated for tumour targeting,[77] including many studies focusing on QDs. For example, folic acid was conjugated to PEG and subsequently deposited onto *N*-acetyl-L-cysteine (NAC)-stabilised CdTeS QDs, which was demonstrated to be able to target tumours in mouse models.[78] Another small targeting molecule is hyaluronic acid, which is widely distributed throughout connective, epithelial, and neural tissues. Hyaluronic acid, associated with tumour angiogenesis and progression,[79] has been conjugated to QDs for tumour targeting, as it can specifically bind with CD44, a cell-surface glycoprotein overexpressed in many tumour types. Therefore their conjugates have not only cancer targeting characteristics, but also the capability for imaging lymphatic vessels.[80]

In addition to the high cost, the low targeting efficacy and the unclear mechanism could also limit their clinical applications. This is because not all cancer cell types overexpress the same unique receptors, and the overexpressed receptors are often present on normal cells.[75] Moreover, the density of the targeted receptors on tumour cells could be another factor influencing the targeting efficacy. For II-VI QDs, the biggest challenge for their clinical applications is their potential toxicity, as discussed in the following section.

2.4 QD toxicity

Most II-VI QDs consist of toxic elements such as cadmium, lead, mercury, etc. Their toxicity has always been of concern and could limit the diversity of their applications, such as in solar cells, light-emitting diodes, flat-screen televisions, and biomarkers.[81] The bio-toxicity depends on multiple factors,[82] which can be mainly classified into two groups: (1) the inherent properties of QDs, including QD size, charge, composition, concentration, and outer-layer coating bioactivity (capping material, functional groups); (2) environmental factors such as oxidation, photolysis, and mechanical effects. A number of studies show that appropriate surface modification, modulating the surface charge, and controlling the QD dosage can effectively reduce QD cytotoxicity. Previously, we demonstrated that coating QDs with silica shells can improve their stability and reduce the

toxicity (Figure 5).[74] Some research has shown that the release of Cd^{2+} and the oxidation products of anions are responsible for their bio-toxicity.[66] The QDs themselves (i.e. non-degraded QDs) are not acutely toxic, and they can be retained in the body for two years and remain fluorescent.

In 2007, Choi and co-workers studied the renal clearance of QDs.[83] They chose cationic, anionic, zwitterionic, and neutral molecules to modify CdSe@ZnS core-shell QDs and tested their binding with serum proteins. They found that the QD surface charge has a profound effect on the adsorption of serum proteins and the hydrodynamic diameter. Cationic or anionic charge led to the hydrodynamic size increasing from around 5 nm to over 15 nm after incubation with serum. Neutral (PEGylated) QDs did not aggregate, but had a large size. Zwitterionic coatings prevented serum protein adsorption and produced the smallest hydrodynamic size. The biodistribution results show that a final hydrodynamic diameter < 5.5 nm resulted in rapid and efficient urinary excretion and elimination of QDs. In their later report, the authors conjugated small targeting molecules on the surface of zwitterionic coatings of QDs.[84] These targeted probes were also cleared by the kidneys when their hydrodynamic size was smaller than 5.5 nm, which sets an upper limit of 5–10 ligands per QD for renal clearance. The animal models demonstrated their performance for *in vivo* targeted imaging and renal clearance within 4 h post-injection.

Recently, Ye *et al.* injected phospholipid micelle-encapsulated CdSe/CdS/ZnS QDs into rhesus macaques, and tracked the relevant markers in the next 90 days.[85] Their results demonstrated that the acute toxicity of these QDs *in vivo* is minimal. Accumulation of an initial dose of Cd was found in the liver, spleen, and kidneys, however, even after 90 days, indicating slow breakdown and clearance of the QDs. Although QDs have not shown acute or short-term toxicity, comprehensive assessments of their long-term bio-toxicity are needed to confirm the ultimate fate of these heavy metals and the impact of their persistence in primates for potential clinical use.

3 Fluorescent metal nanoclusters

Since QDs have potential toxicity and long *in vivo* retention time, many efforts have been made to develop alternatives to them. An alternative is fluorescent metal nanoclusters, which have attracted considerable attention during the past several years. It is well known that large nanoparticles of metals such as Au, Ag, and Cu possess the face-centred cubic (fcc) structure and the surface plasmon resonance (SPR) property.[86] Their SPR absorption is due to the collective oscillation of electrons on the surfaces, and it is strongly dependent on the particle size. When that size is smaller than the electron mean path (e.g. 20 nm for Au nanoparticles), the conducting electrons in the ground states and excited states are confined.[86] The large metal nanoparticles have very low fluorescence emission. Very interestingly, when their size is further reduced below 2 nm, the ultra-small nanoclusters possess different crystal structures and exhibit strong photoluminescence while their unique SPR property disappears.

Nanoclusters bridge the gap between molecules and nanoparticles, and could simultaneously display the properties of both molecules and nanoparticles. Their novel optical, electronic,

and catalytic activities make them very useful in ultrasensitive detection, biolabelling, bioimaging, and catalysis.[87-90] The big challenge, however, is how to controllably synthesize metal nanoclusters with defined size, composition, crystal structure, and surface properties.[88, 91]

3.1 Synthesis of fluorescent metal nanoclusters

Compared with large nanoparticles, metal nanoclusters are difficult to synthesize and functionalize because they only consist of a few to tens of metal atoms. They are very sensitive to slight variation of the environment, such as solution pH, ion strength, solvents, oxygen, temperature etc. They have very high surface-area-to-volume ratios and tend to aggregate into large particles. In general, fluorescent metal nanoclusters can be prepared by reduction of metal precursors or etching of large nanoparticles in the presence of strong stabilizers such as small thiol-molecules, polymers, and biomolecules.

Reduction of metal precursors such as salts and complexes is a straightforward way to produce fluorescent metal nanoclusters. Au nanoclusters are usually chosen as representative for investigation due to their high chemical stability, easy preparation, and biocompatibility. The first observation of Au photoluminescence from its ingots, single-crystal slices, and films, with a QY of 10^{-10}, was reported by Mooradian in 1969.[92] The extremely low QY did not attract any attention until Wilcoxon *et al.* observed fluorescence from colloidal Au nanoparticles with a QY of $10^{-5} - 10^{-4}$.[93] The authors prepared colloidal Au nanoparticles through reduction of $HAuCl_4$ by citrate in water, or by metallic sodium dispersion or lithium trisamylborohydride in inverse micelles, and then used liquid chromatography to fractionate the resultant Au nanoparticles. They found that only nanoparticles smaller than 5.0 nm showed a blue fluorescence at 440 nm under an excitation of 230 nm. Their results suggest that ultra-small nanoclusters could exhibit strong fluorescence.

A breakthrough in preparing fluorescent Au nanoclusters was achieved by Zheng and co-workers.[94-96] They synthesized a series of Au_5, Au_8, Au_{13}, Au_{23}, and Au_{31} nanoclusters using poly(amidoamine) (PAMAM) dendrimers as stabilizers. By adjusting the molar ratio between Au^{3+} and PAMAM from 1:1 to 1:15, they tuned the emission of these Au nanoclusters from the ultraviolet (UV) to the near infrared (NIR) range with a QY from 10% to 70%. The latter experiments, however, proved that PAMAM dendrimers made a contribution to the solution fluorescence. The authors also used dendrimers as ligands to prepare fluorescent Ag nanoclusters.[89, 97] In addition to dendrimers, some other polymers such as multiarm star polyglycerol-block-poly(acrylic acid) and DHLA functionalized PEG were used to stabilize metal nanoclusters. [98, 99]

Recently, we used multidentate thioether-terminated poly(methacrylic acid) (PTMP-PMAA) (Figure 7(a)) as ligand to successfully prepare water-soluble fluorescent Au nanoclusters through reduction of $HAuCl_4$ with $NaBH_4$.[100] Due to the strong steric effect, this polymer ligand has also been used to prepare ultra-small magnetic iron oxide nanoparticles.[101-104] By controlling the polymer concentration and molecular weight, we obtained a series of Au nanoclusters with emissions between 540 – 800 nm and QYs of 2.6 – 4.8%. In contrast to dendrimers, our
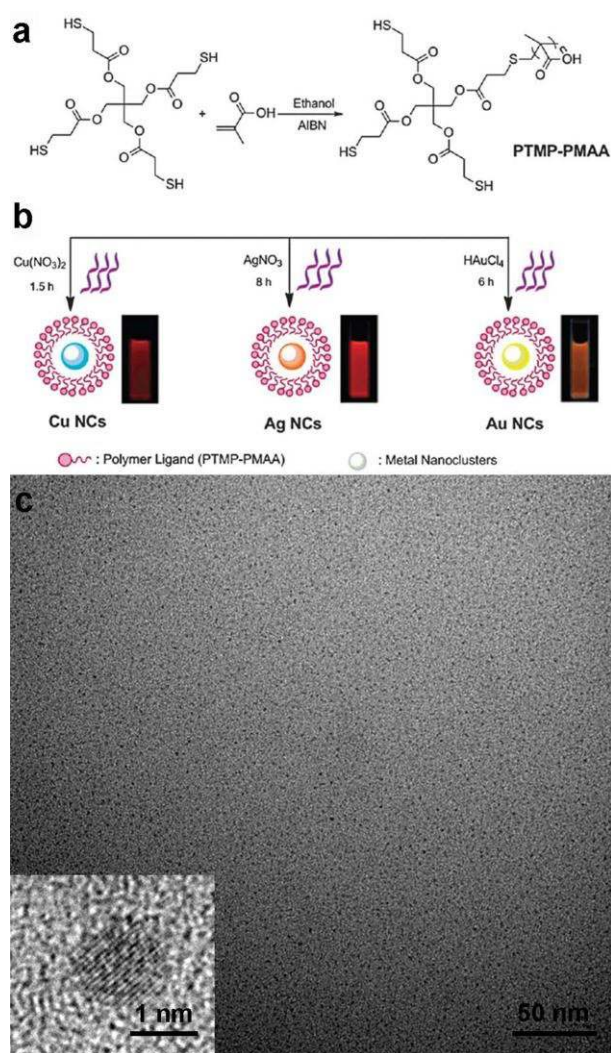

Figure 7. Schematic diagram of preparation of **(a)** polymer ligand PTMP-PMAA; **(b)** photoreductive synthesis of fluorescent Cu, Ag, and Au nanoclusters; **(c)** TEM image of Au nanoclusters. Reproduced from Ref. 100 and Ref. 105.

polymer ligands did not show fluorescence, and the observed fluorescence was only caused by the Au nanoclusters. The different emissions of Au nanoclusters are attributed to their different sizes. On the basis of this research, we prepared fluorescent Au, Ag, and Cu nanoclusters using photoreduction rather than chemical reduction (Figure 7(b)).[105] Compared with conventional chemical reduction, photoreduction is clean and non-toxic as this method avoids the use of additional reducing agents. The QYs of the resultant Au, Ag, and Cu nanoclusters were 5.3%, 6.8%, and 2.2%, respectively. Using the photoreduction method, Shang *et al.* also prepared very highly fluorescent Ag nanoclusters (18.6% QY) in the presence of poly(methacrylic acid) (PMAA).[106]

Compared with PMAA, our polymer ligands have a stronger steric hindrance effect. Figure 7(c) presents a typical transmission electron microscope (TEM) image of Au nanoclusters stabilized with PTMP-PMAA, clearly showing their ultra-small size (< 1.0 nm). In order to further investigate the polymer hindrance effect, we designed three types of tridentate thioether-terminated

polymer ligands,[107] i.e. poly(methyl methacrylate) (PTMP-PMMA), poly(n-butyl methacrylate) (PTMP-PBMA), and poly(t-butyl methacrylate) (PTMP-PtBMA), which were used to synthesize fluorescent Au nanoclusters through the facile photoreduction method. The resultant Au nanoclusters exhibited blue fluorescence instead of red fluorescence due to their small particle size. Their QYs were found to be 3.8%, 14.3%, and 20.1%, respectively, which increases with increasing polymer steric hindrance, i.e. PTMP-PMMA < PTMP-PBMA < PTMP-PtBMA.

In addition to polymer ligands, small thiol molecules such as glutathione, tiopronin, MPA, DHLA, phenylethylthiolate, and thiolate α-cyclodextrin were also used to prepare fluorescent metal nanoclusters.[87, 108, 109] For example, Luo *et al.* used L-glutathione as ligands to prepare Au(0)@Au(I)-thiolate core-shell nanoclusters with a QY of 15%.[109] They proposed that strong luminescence emission is attributed to aggregation-induced emission of Au(I)-thiolate complexes. The QYs of metal nanoclusters stabilized by small molecules are similar to those nanoclusters stabilized with polymer.

In order to improve the biocompatibility of fluorescent metal nanoclusters, several groups used biomolecules such as oligonucleotides, peptides, and proteins as stabilizers during preparation.[110-113] For example, the Dickson group took advantage of the strong affinity of Ag$^+$ to cytosine bases from single-stranded DNA, and prepared very small Ag nanoclusters using DNA as stabilizer.[110] In their later report, they used DNA microarrays for high-throughput analysis of 12-mer strands to identify optimized sequences for Ag encapsulation, and produced five distinct Ag emitters with QYs in the range of 16 – 34%.[111] Compared with single-stranded DNA, proteins have abundant binding sites and offer better protection to metal nanoclusters. Xie *et al.* prepared Au$_{25}$ nanoclusters with a QY of 6.0% using bovine serum albumin (BSA) as the stabilizer and reducing agent.[112] The reduction process was induced by adjusting the solution pH.

Similar to the QDs produced in living organisms, fluorescent metal nanoclusters can also be formed *in-situ* in cells. For example, Wang and co-workers found that fluorescent Au nanoclusters were spontaneously biosynthesized by cancer cells (human hepatocarcinoma cell line HepG2 and leukaemia cell line 562) rather than normal cells such as human embryo liver cells (L02) when the cells were incubated with chloroauric acid solution.[114] Au nanoclusters were formed by reduction of Au-precursor inside the cell cytoplasm and concentrated around their nucleoli. The selective formation of fluorescent Au nanoclusters by cancer cells can be exploited for *in vivo* self-bio-imaging of tumours.

Etching of large metal nanoparticles is an alternative approach to prepare fluorescent metal nanoclusters. The etching process can be performed by adding strong ligands or precursors into the nanoparticle solution. For example, Muhammed *et al.* synthesized fluorescent Au nanoclusters from MSA-stabilized Au nanoparticles by etching with excess glutathione.[115] The etching process is pH-dependent and the obtained Au$_8$ and Au$_{25}$ nanoclusters have a QY of 0.015% and 0.19%, respectively. They also developed an interfacial etching process to prepare fluorescent Ag nanoclusters.[116] First, they prepared MSA-
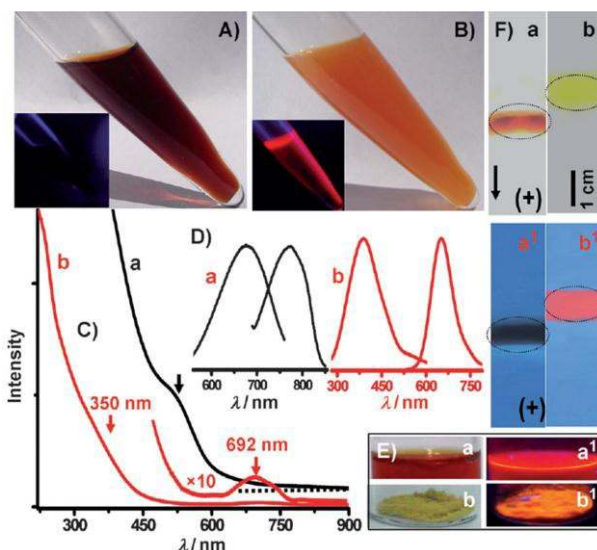

Figure 8. (A-B) Solutions of Ag$_{7,8}$ and alloyed Ag$_7$Au$_6$ nanoclusters; **(C-D)** their absorption and emission spectra; **(E)** alloyed Ag$_7$Au$_6$ nanoclusters in solution and in the solid state under visible and UV light; **(F)** comparison of the PAGE of Ag$_{7,8}$ and alloyed Ag$_7$Au$_6$ nanoclusters. Reproduced from Ref. 117.

stabilized Ag nanoparticles and then added them into an organic solvent (e.g. toluene, carbon tetrachloride, diethyl ether) containing excess MSA under magnetic stirring. A mixture of Ag$_8$ and Ag$_7$ nanoclusters with red and blue-green fluorescence was obtained. The QYs of the Ag$_8$ nanoclusters at room temperature and 273 K were calculated to be 0.3% and 9%, respectively. The authors used a similar approach to obtain alloyed Ag$_7$Au$_6$ nanoclusters (3.5% QY) by adding HAuCl$_4$ solution into the as-etched Ag nanocluster solution (Figure 8).[117]

In addition to small molecules, multivalent polymers can also be used as etching agents. Duan *et al.* used multivalent polyethylenimine (PEI) to etch 8 nm Au nanoparticles, which were prepared by a two-phase approach and stabilized with dodecylamine. The resultant cluster solution surprisingly appeared to be in an oxidized electronic state with an emission at 505 nm. The emission was blue shifted to 445 nm with a QY of 10 - 20% after reduction with NaBH$_4$.[118]

Similar to organic ligands, metal precursors can also induce the etching process. For example, Lin and co-workers extracted HAuCl$_4$ from aqueous solution into didodecyldimethylammonium bromide (DDAB) toluene solution, and then added the mixture into 5.6 nm Au solution to result in 3.2 nm particles.[119] After replaced DDAB with dihydrolipoic acid, these Au nanoparticles were further decreased to 1.6 nm and showed a red emission around 700 nm. Their fluorescence QY was 3.4% in methanol and 1.8% in water (pH = 9). Recently, Yuan *et al.* developed a general etching approach to prepare fluorescent Au, Ag, Cu and Pt nanoclusters with a QY of 5.4%, 6.5%, 3.5% and 4.6%, respectively.[120] They started with glutathione-stabilized metal nanoparticles, and then transferred the metal nanoparticles into an organic phase by taking advantage of the electrostatic interactions between negatively charged glutathione (carboxyl group) and positively charged cetyltrimethylammonium bromide (CTAB). The beauty of this

approach is that the resultant fluorescent metal nanoclusters can be shuttled back to the aqueous phase using hydrophobic-hydrophobic interactions upon addition of hydrophobic salts (e.g. tetramethylammonium decanoate) in chloroform.

Besides these methods, microwaves and ultrasound were also used to assist the synthesis of fluorescent metal nanoclusters in recent years.[121, 122] For example, Xu and Suslick adopted sonochemistry to prepare fluorescent Ag nanoclusters with a QY of 11% in the presence of PMAA.[121] Shang *et al.* synthesized fluorescent Au nanoclusters (2.9% QY) via a rapid microwave assisted method.[122] In all syntheses, ligands play a crucial role in obtaining these ultra-small fluorescent metal nanoclusters. Their ability to donate electrons drastically influences the fluorescence intensity, i.e. the stronger the electron donating capability is, the higher the fluorescence intensity will be. [123]

3.2 Characterization and modification of fluorescent metal nanoclusters

Metal nanoclusters can be characterized by the techniques applied to nanomaterials and molecules. Compared with large nanoparticles, metal nanoclusters have a smaller size and a "narrower" size distribution, so that size-selective precipitation is not suitable for their separation. They are usually fractionated by chromatography and electrophoresis techniques, which are usually applied to molecules. These separation methods include high-performance liquid chromatography (HPLC), size exclusion chromatography (SEC), ion exchange chromatography (IEC), capillary electrophoresis, and polyacrylamide gel electrophoresis (PAGE). It is still very challenging to obtain monodisperse nanoclusters using these approaches. For example, Tsunoyama *et al.* separated Au:SC$_x$ nanoclusters into different fractions using gel permeation chromatography (GPC),[124] and then characterized them with laser-desorption ionization (LDI) mass spectroscopy. The results show that each fraction had a wide distribution of Au atoms although they were well separated with high resolution in the GPC spectrum. Negishi and co-workers synthesized glutathione-protected Au nanoclusters and then fractionated them into 9 fractions, with the number of Au atoms ranging from 10 to 39 by PAGE analysis.[125] Among their Au nanoclusters, Au$_{25}$(SG)$_{18}$ is the most stable one.

The size of fractionated metal clusters can be characterized by TEM, and their molecular weight can be measured by mass spectroscopy. In principle, their crystal structures could be determined by X-ray diffraction (XRD). Metal nanoclusters are less ordered, however, and their powder XRD patterns are broad. In comparison with metal complexes with defined molecular structure, it is very difficult to obtain single crystal clusters for structural characterization. So far, most structural investigations of metal nanoclusters are focused on "large" Au nanoclusters.[91, 108, 126-128] For example, Jadzinsky *et al.* determined the structure of a Au$_{102}$(*p*-mercaptobenzoic acid)$_{44}$ single crystal and found a core-shell structure,[127] in the which the Au$_{49}$ core is surrounded by two groups of Au atoms. Qian and co-workers characterized the crystal structure of Au$_{25}$(SR)$_{18}$ and Au$_{38}$(SR)$_{24}$ nanoclusters, and found a similar core-shell structure.[91] An Au$_{25}$(SR)$_{18}$ cluster consists of an icosahedral Au$_{13}$ core and exterior 12 Au atoms in the form of six –RS–Au–RS–Au–RS– motifs.[91, 108]
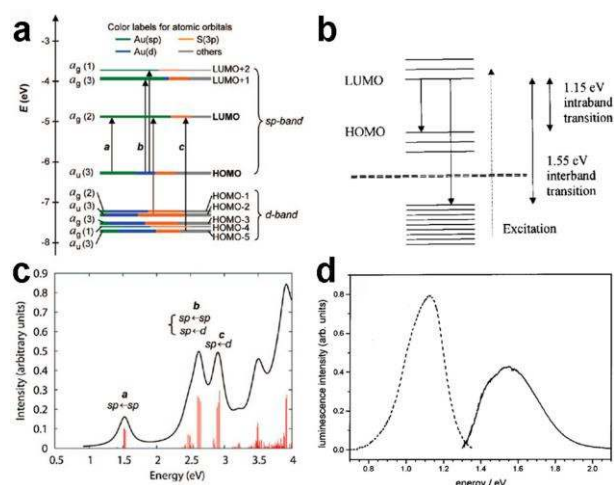

Figure 9. (a) Kohn-Sham orbital energy level diagram for a model compound Au$_{25}$(SH)$_{18}$; **(b)** Solid-state model for the origin of the two luminescence bands in (d); **(c)** theoretical absorption spectrum of Au$_{25}$(SH)$_{18}$; **(d)** two luminescence peaks observed in Au$_{28}$(SG)$_{16}$ clusters. Reproduced from Ref. 131 and Ref. 132.

The ultra-small size (limited atomic numbers) of metal nanoclusters makes it possible to predict their crystal structures through precise theoretical simulation. For example, Xiang *et al.* developed a new genetic algorithm approach to search for the global lowest-energy structures of DMSA-stabilized Ag nanoclusters.[129] In combination with density functional theory (DFT), their genetic algorithm simulations show that the ground state of [Ag$_7$(DMSA)$_4$]$^-$ has eight instead of four Ag–S bonds, with a much lower energy than the structure based on the [Ag$_7$(SR)$_4$]$^-$ cluster with a quasi-two-dimensional Ag$_7$ core. Their simulated X-ray diffraction pattern of the [Ag$_7$(DMSA)$_4$]$^-$ cluster is in good agreement with the experimental results.

The optical properties of fluorescent metal nanoclusters can be characterized with UV-visible (UV-Vis) absorption and photoluminescence spectroscopy. As mentioned previously, metal nanoclusters have no SPR absorption, but they show molecular-like electronic transitions due to the quasi-continuous energy band structure and quantum confinement effects. Bakr *et al.* synthesized Ag nanoclusters through the reduction of Ag-precursor in the presence of 4-fluorothiophenol,[130] and investigated the evolution of their absorption from multiple bands into a single SPR band by heating the original nanocluster solution at 90 °C for different periods of time. Their results demonstrate the size dependence in UV-Vis absorptions of metal nanoclusters.

In order to demonstrate the origin of multiband absorption, Zhu and co-workers chose the Au$_{25}$(SR)$_{18}$ cluster as a model and simulated their absorption by performing time-dependent DFT calculations.[131] Figure 9(a) shows the Kohn-Sham molecular orbitals, energies, and atomic orbital contributions in the cluster. The highest occupied molecular orbital (HOMO) and the lowest three lowest unoccupied molecular orbitals (LUMOs) are mainly composed of 6*sp* atomic orbitals of Au, and these orbitals constitute the *sp*-band. The HOMO-1 to HOMO-5 orbitals are constructed from the 5*d* atomic orbitals of Au and form the *d*-band. In addition, the *s* 3*p* orbitals make contributions to both sets of HOMO and LUMO orbitals. The multiband absorption of

metal nanoclusters suggests their multiple emission peaks and broad fluorescence spectra (Figure 9(b)). Figure 9(c) shows the simulated absorption spectrum. The multiple absorptions are attributed to the intraband (sp) HOMO → LUMO transition, the interband transition ($d \rightarrow sp$), or mixed $sp \rightarrow sp$ intraband and $d \rightarrow sp$ interband transitions.[131] Figure 9(d) shows two fluorescence bands with the maxima at around 1.5 and 1.15 eV observed in $Au_{28}(GSH)_{16}$ nanoclusters by Link et al.[132] These two bands are separated from a broad luminescence in the range of 2.0 – 0.8 eV, and are ascribed to the radiative interband recombination between the sp and d bands, and intraband transitions (sp bands) between the HOMO and LUMO.

Despite the good agreement between simulated data and experimental observations, the origin of metal fluorescence is not completely understood. Most reported atomically precise $Au_n(SR)_m$ nanoclusters show very weak luminescence. Recently, Yu and co-workers identified that $Au_{22}(SR)_{18}$ has two RS-[Au-SR]$_3$ and two RS-[Au-SR]$_4$ motifs that are interlocked and capped on a prolate Au8 core.[133] These $Au_{22}(SR)_{18}$ nanoclusters exhibited an emission at ~665 nm with a QY of ~8%. Their results show that the luminescence of these core-shell nanoclusters was generated by the aggregation-induced emission of Au(I)-thiolate complexes on the nanocluster surface.

The fluorescence of metal nanoclusters is very sensitive to the cluster size, surface ligands, solvents, etc., so it is thus necessary to modify them in order to maintain their bright fluorescence in addition to improving their stability and biocompatibility. There are few reports, however, on the post-modification of fluorescent metal nanoclusters in comparison with large nanoparticles, due to their tiny size and sensitivity to external conditions. Lin and co-workers prepared DHLA-protected fluorescent Au nanoclusters by etching large nanoparticles and replacing surface ligands.[119] They took advantage of carboxylic acid groups from DHLA to conjugate PEG–NH$_2$ or biotin-PEG–NH$_2$ with Au nanoclusters. The gel electrophoresis and the cell labelling indicate the successful conjugation. Samanta et al. prepared fluorescent Au nanoclusters using a novel quaternary ammonium as the ligand, and then coated them with silica.[134] Similar to fluorescent QDs, surface modification can lead to the fluorescence quenching of metal nanoclusters. It is still a great challenge to obtain robust fluorescent metal nanoclusters through surface modification.

3.3 Application of fluorescent metal nanoclusters in bioimaging

Similar to other fluorophores, fluorescent metal nanoclusters have also been tested for in $vitro$ and in $vivo$ bioimaging. In the early reports, Zheng et al. prepared fluorescent Au, Ag nanoclusters in the presence of dendrimers, DNA, and proteins, and used them as labels for cell imaging.[89, 94-97] Baskov et al. prepared fluorescent Ag nanoclusters in the presence of thioflavin T with remarkable fluorescent properties,[135] and then used them to label amyloid fibrils produced from recombinant mammalian prion proteins and non-prion proteins. The labelled amyloid fibrils exhibited a time-dependent increase in fluorescence with no photobleaching after 24-h illumination, while those stained with thioflavin T showed a rapid decay in fluorescence. Their results demonstrate the higher stability of Ag nanoclusters than that of organic fluorophore.

Recently, we prepared fluorescent Au nanoclusters stabilized with PTMP-PMAA, and then compared them with CdTe QDs in
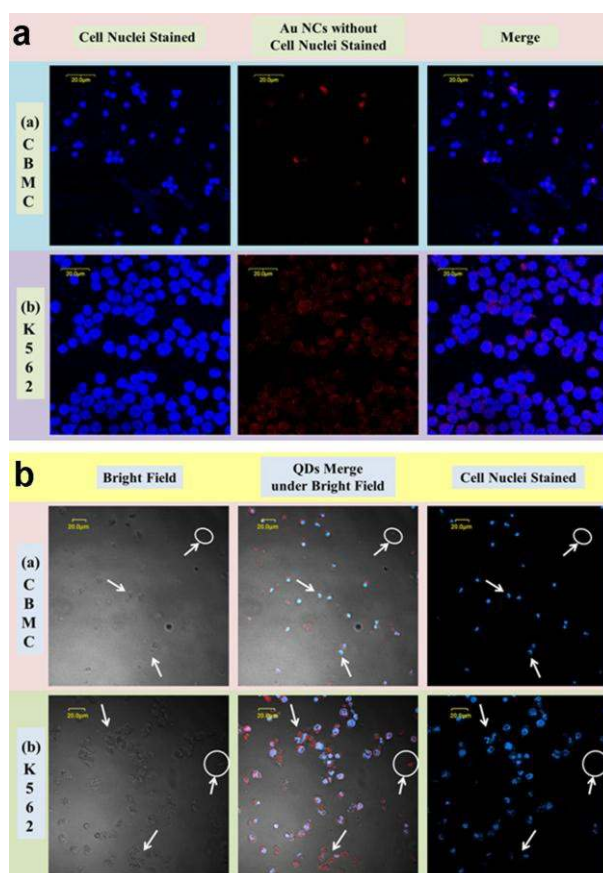

Figure 10. Comparison of cell labeling by using fluorescent Au nanoclusters and CdTe QDs. Reproduced from Ref. 100.

labelling suspended and adherent hematopoietic relatively normal cord blood mononuclear (CBMC) cells and cancer K562 cells (Figure 10).[100] The results show that the cancer cells took up more Au nanoclusters than the normal cells, even though they were from the same hematopoietic system. There was no difference, however, in the uptake of CdTe QDs between the two kinds of cells. The selective uptake of Au nanoclusters by cancer cells could be attributed to the unique properties of Au nanoclusters or the nature of the cells. In addition, CdTe QDs destroyed the nuclei of some cells. We also compared the cytotoxicity of Au nanoclusters with that of CdTe QDs through MTT and apoptosis assay. The results show that our fluorescent Au nanoclusters had lower toxicity than QDs, and did not induce acute toxicity. These advantages make them very attractive in selective bio-labelling of cancer cells. Retnakumari et al. conjugated folic acid with BSA-stabilized Au nanoclusters and then used them for targeted imaging.[136] The receptor-targeted cancer detection was demonstrated on FR^{+ve} oral squamous cell carcinoma (KB) and breast adenocarcinoma MCF-7 cells, where the FA-conjugated Au_{25} clusters were found to be internalized in significantly higher concentrations compared to the negative control cell lines.[136] Apart from routine utilization of cell labelling, fluorescent metal nanoclusters can be used as intracellular sensors. For example, Shang and co-workers demonstrated the use of Au nanoclusters for intracelluar thermometry by taking advantage of the temperature sensitivity of their fluorescence lifetime and emission intensity (Figure
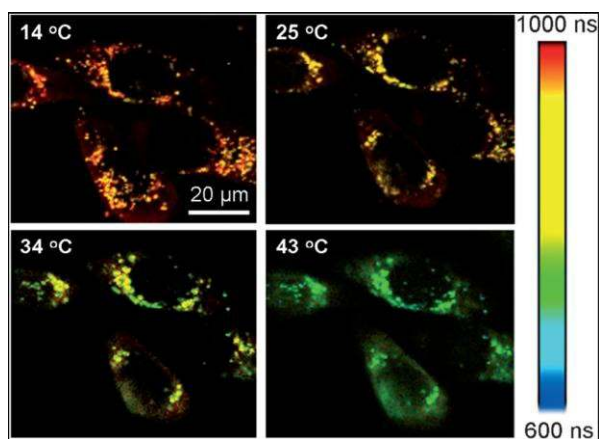
Figure 11. FLIM images of HeLa cells with internalized Au nanoclusters at four different temperatures. Reproduced from Ref. 15.

Figure 12. (a) Biodistibution of 2-nm GS-Au nanoclusters. The inset shows CT images of a live mouse before and 30 min after injection of Au nanoclusters; **(b-d)** comparison of biodistribution of GS-Au nanoclusters and IRDye 800CW. Reproduced from Ref. 138 and Ref. 139.

11).[15] Using fluorescence lifetime imaging microscopy (FLIM), they observed the considerable variation of fluorescence lifetime of nanoclusters internalized in HeLa cells with the temperature increasing from 15 to 45 ˚C.

5 In addition to the above *in vitro* cell labelling and imaging, Wu *et al.* investigated *in vivo* imaging through the tail vein administration of near infrared (NIR) fluorescent Au nanoclusters in live mice,[137] and found that the uptake of NIR Au nanoclusters by the reticuloendothelial system was relatively low in
10 comparison with other nanoparticles due to their ultra-small hydrodynamic size (~2.7 nm). They then used MDA-MB-453 and xenografted HeLa tumour cells as models to do *in vivo* and *ex vivo* imaging studies, and found that the ultra-small Au nanoclusters were highly accumulated in the tumour areas due to
15 the enhanced permeability and retention (EPR) effect.[137]

Zhou and co-workers studied the renal clearance of 2 nm glutathione (GSH)-coated fluorescent Au nanoclusters (Figure 12),[138] and found that only ~4% of the particles were accumulated in the liver, while more than 50% of the particles were found in
20 urine within 24 h after intravenous injection, which is comparable to the QDs with the best renal clearance efficiency.[83] They also used computed tomography (CT) to visualize real time accumulation of luminescent GS-AuNPs in the bladder, and demonstrated that fluorescent Au nanoclusters can serve as
25 contrast agents for CT imaging (Figure 12). Recently, they compared GSH-coated fluorescent Au nanoclusters (2.5 nm) with small dye molecules IRDye 800CW,[139] and found that they both have similar physiological stability and renal clearance, but Au nanoclusters exhibited a much longer tumour retention time and
30 faster normal tissue clearance (Figure 12). These merits enabled the Au nanoclusters to detect the tumour more rapidly than the dye molecules without severe accumulation in reticuloendothelial system organs.[139]

Besides the above *in vivo* passive targeting, fluorescent metal
35 nanoclusters can be tagged with bioactive molecules for targeting, imaging, and therapy. For example, Liu *et al.* synthesized fluorescent Au nanoclusters (0.92 ± 0.03 nm) using insulin as a template.[113] The resulting Au-insulin nanoclusters retain the insulin bioactivity and biocompatibility, and have been used to
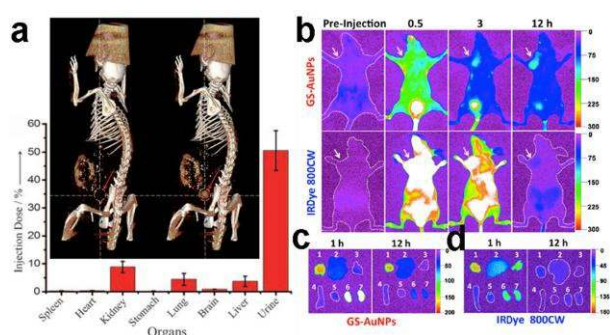40 regulate the *in vivo* glucose level in Wistar rats. The results show that an injection of insulin-Au nanoclusters into the rats tended to reduce the blood glucose in a similar way to commercial insulin. Fluorescent insulin-Au nanoclusters can also be used as contrast agents for CT imaging.[113] These studies indicate that ultra-small
45 fluorescent Au nanoclusters could simultaneously serve as very promising contrast agents for *in vivo* fluorescence imaging and CT imaging.

In summary, fluorescent metal nanoclusters as emerging fluorophores have attracted considerable attention due to their
50 tuneable emissions, ultra-small size, fast renal clearance, and low toxicity. There are a few obstacles to be overcome, however, including (i) low fluorescence QY, which is usually about ~10% and less than that of QDs and many organic dyes; (ii) polydispersity in size and components, which makes it very
55 difficult to fundamentally study their novel properties and mechanisms; (iii) difficulty in modifying their surface to introduce other functions due to their tiny size and lower stability; (iv) complicated interactions with biological environments.

60 **4 Fluorescent carbon nanomaterials**

4.1 Fluorescent carbon dots

Fluorescent carbon dots are also used as alternatives to QDs for bioimaging,[17, 140] because they not only exhibit several favourable attributes of traditional semiconductor-based QDs (namely, size-
65 and wavelength-dependent emission, resistance to photobleaching, ease of bioconjugation), but also show chemical inertness, low toxicity, and biocompatibility. Fluorescent carbon dots were accidently discovered in 2004 during the purification of single-wall carbon nanotubes (SWCNTs) fabricated by the arc-
70 discharge approach.[141] Two new classes of nanomaterials were isolated from the crude soot. One was short, tubular carbon, and the other a mixture of fluorescent nanoparticles derived from the SWCNTs.

In 2006, Sun *et al.* obtained 5-nm non-fluorescent carbon dots
75 via laser ablation of a carbon target, and then modified them with PEG to get fluorescent carbon dots with a fluorescence QY of 4% – 10%.[142] The photoluminescence of these carbon dots was broad and strongly dependent on the excitation wavelength, which could be attributed to the different sizes in the sample and
80 different emission sites on the passivated particle surfaces. After fractionation with gel column chromatography, most of the
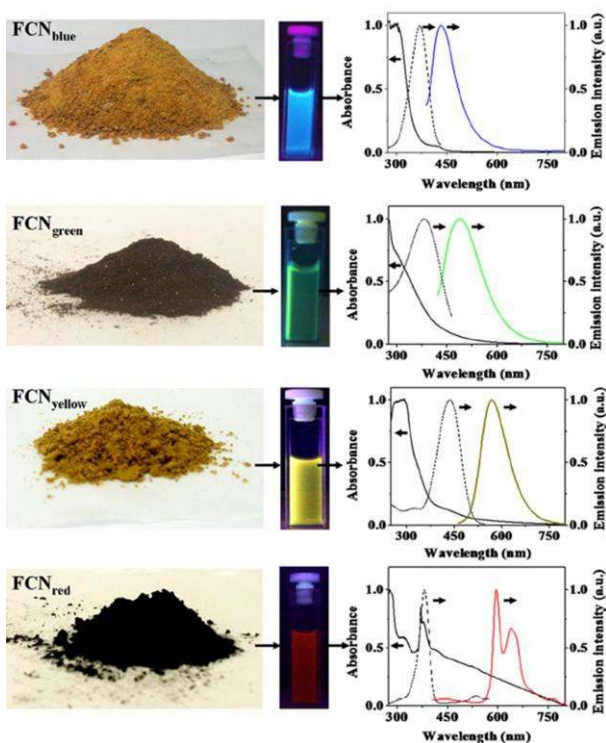
Figure 13. Digital images of solid fluorescent carbon dots, aqueous solutions, and their absorption, excitation and emission spectra. Reproduced from Ref. 144.

Figure 14. (a) NIR images of mouse bladders acquired before and after injection of carbon dots through intravenous injection, subcutaneous injection, and intramuscular injection; (b) quantification of the ZW800 fluorescence signal in (a); (c) representative coronal images from 1 h dynamic positron emission tomography (PET) imaging. Reproduced from Ref. 152.

fluorescent fractions could achieve emission yields close to 60 %.[143] Interestingly, their optical properties resemble band-gap transitions, which are found in nanoscale semiconductors, suggesting that carbon dots have essentially semiconductor-like characteristics. Recently Bhunia *et al.* prepared hydrophobic and hydrophilic carbon dots with tuneable size and visible emissions,[144] by dehydrating carbohydrate in octadecene in the presence of octadecylamine, or in concentrated sulphuric acid (Figure 13). Their method produced gram-scale fluorescent carbon dots with a QY of 6 – 30%. Zhu and co-workers also reported a rapid and high-output hydrothermal approach to prepare polymer-like carbon dots with QYs as high as 80 %.[145]

In addition to solid fluorescent carbon dots, there are some reports on hollow fluorescent carbon dots.[146, 147] For example, Fang *et al.* simply mixed acetic acid, water and diphosporus pentoxide to obtain cross-linked hollow fluorescent carbon nanoparticles. By reducing the release of heat, they also obtained solid fluorescent nanoparticles. So far, many approaches, such as arc-discharge, laser ablation, electrochemical oxidation, combustion/pyrolysis, and hydrothermal and microwave methods, have been developed to prepare solid and hollow fluorescent carbon dots.[148] The preparation is inexpensive on a large scale without the need for stringent, intricate, tedious, costly, or inefficient steps.[149] The recent advances in the synthesis and characterization of fluorescent carbon dots have been reviewed.[17, 148, 149]

The first study of fluorescent carbon dots in bioimaging was reported by the Sun group in 2007.[150] The authors used poly-(propionylethylenimine-*co*-ethylenimine) (PPEI-EI, with EI fraction ~20%) to modify the carbon dots, and then applied them to label human breast cancer MCF-7 cells. These labelled cells
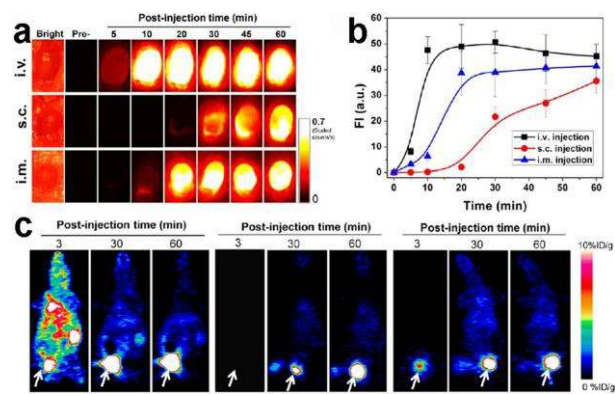
exhibited bright fluorescence in both cell membrane and cytoplasm regions under an excitation of 800-nm laser pulses. The results demonstrate that carbon dots exhibit strong luminescence with two-photon excitation in the near-infrared, and moreover, large two-photon absorption cross-sections, comparable to those of available high-performance semiconductor QDs.[150] The authors further demonstrated the *in vivo* imaging of fluorescent carbon dots.[151] They compared the imaging capability of carbon dots and ZnS-doped carbon dots, and found that the later dots emitted more strongly than the former dots both in solution and in mice. The fluorescence from the bladder area was observed, and 3 h after injection, the fluorescence could be detected in the urine, but it completely faded 24 h after injection. They analysed the biodistribution of carbon dots and found that the carbon dots accumulated in the kidney and, to a small extent, in the liver.[151] This is attributed to the surface PEG, which likely reduces the protein adsorption.

Recently Huang and co-workers investigated the effects of injection routes on the biodistribution, clearance, and tumour uptake of carbon dots (Figure 14).[152] They prepared fluorescent carbon dots through a laser ablation approach, and then functionalized carbon dots with the NIR dye ZW-800 and the isotope [64]Cu. They injected the conjugates into mice in three different manners, i.e. intravenous, intramuscular, and subcutaneous injection. The results show that the carbon dots were efficiently and rapidly excreted from body after injection, and the clearance rate of carbon dots decreased when the administration was varied from intravenous, to intramuscular, and then to subcutaneous injection (Figure 14). Different injection routes also showed different blood clearance patterns and different tumour uptake of carbon dots.

4.2 Fluorescent graphene quantum dots

It should be noted that fluorescent graphene quantum dots (GQDs), the analogues of carbon dots, have also attracted considerable attention.[153, 154] Similar to carbon dots, GQDs can be prepared by top-down and bottom-up approaches, and their fluorescence can be enhanced via surface modification. The top-down methods usually refer to cutting larger size carbon
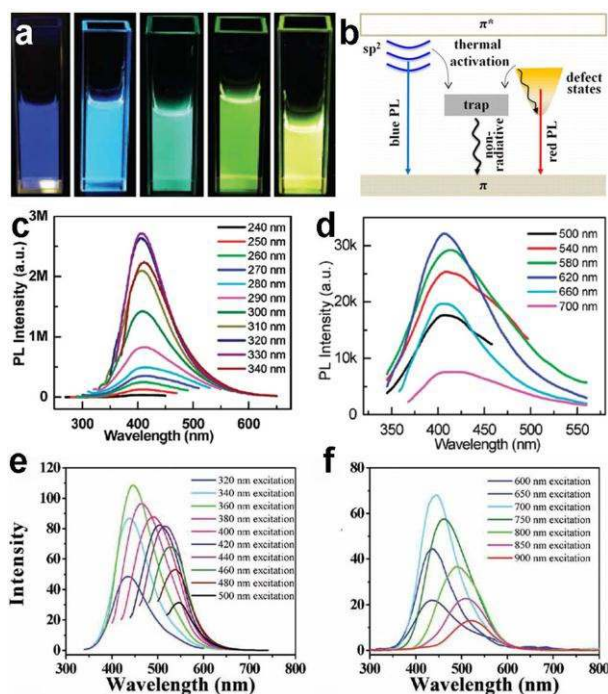
Figure 15. (a) Image of GQD solution under UV-light; (b) schematic emissions in GQDs; (c-d) excitation-independent down-conversion and up-conversion spectra of GQDs; (e-f) excitation-dependent down-conversion and up-conversion spectra of GQDs. Reproduced from Refs. 155, 157, 160, and 161.

Figure 16. Nitrogen-doped GQDs for cellular and deep-tissue imaging. Reproduced from Ref. 164.

materials such as carbon nanotubes, graphene or graphene oxide sheets, and carbon fibres into small GQDs, through strong acid oxidation, hydrothermal or solvothermal treatment, or microwave and sonication treatment.[154] For example, Zhu *et al.* dispersed graphene oxide in dimethyl formamide (DMF) under sonication, and then transferred the suspension into Teflon autoclaves and treated them at high temperature for a few hours to get GQDs with a QY of 11%.[155, 156] Tetsuka and co-workers used the hydrothermal approach to treat graphene oxide sheets in ammonia solution to get GQDs with a QY between ~19 – 29%.[157] The emission of GQDs can be tuned by controlling the hydrothermal temperature (Figure 15(a)), and the QYs can be further enhanced to ~46% after modification with PEG. Wu *et al.* used a one-step pyrolysis of a natural amino acid (i.e. glutamic acid) to prepare fluorescent GQDs with a QY of 54.5%.[158] Recently, Dong and co-workers used L-cysteine as precursor to prepare S,N-co-doped GQDs with a QY up to 73%,[159] which is the highest value reported so far.

The preparation process significantly influences the optical properties of GQDs. There are two types of emissions in GQDs, i.e. intrinsic state emission and defect state emissions (Figure 15(b)).[160] The competition between these two states could be changed during preparation or post surface modification. For example, Zhuo and colleagues oxidized graphene in concentrated H_2SO_4 and HNO_3, and then sonicated the mixture and calcined it at 350 °C to remove acid.[161] The resultant fluorescent GQDs did not exhibit excitation-dependent fluorescence [Figure 15(c-d)].[161] However, Zhu *et al.* prepared green fluorescent GQDs through the hydrothermal approach.[155] The green fluorescence
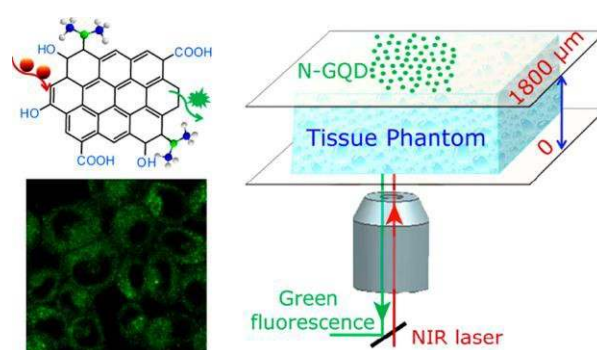
was changed into blue after the GQDs were modified with alkylamines or reduced with $NaBH_4$ (referred to as *m*-GQDs and *r*-GQDs respectively), while the particle size was similar. The fluorescence shift was attributed to the suppression of non-radiative processes and to the enhanced integrity of the π conjugated system. These three types of GQDs exhibited strong excitation-dependent down-conversion and up-conversion emissions, demonstrated by that of the *m*-GQDs in Figure 15(e-f),[155] which is in contrast to Zhuo's report [Figure 15(c-d)]. In addition to the preparation, the optical properties of GQDs are also influenced by the solution pH, solvent, and concentration.[154] Recently, Xu *et al.* studied the fluorescence of GQDs on a substrate at the single particle level.[160] All the GQDs investigated had the same spectral lineshapes and peak positions, despite notable differences in particle size and the number of layers. GQDs with more layers were brighter than those with fewer layers, but were associated with shorter fluorescence lifetimes.

Although there are some debates on the fluorescence mechanisms of GQDs, their unique properties afford many applications in cellular and deep-tissue imaging. Sun and co-workers demonstrated the first bioapplication of nanographene oxide (NGO),[162] i.e., single-layer graphene oxide sheets a few nanometers in lateral width. The PEGylated NGO sheets used were soluble in buffers and serum without agglomeration, and showed photoluminescence in the visible and infrared regions. These NGO sheets had low background photoluminescence in the near-infrared (NIR) window. In addition, simple physisorption through π-stacking was used to load the anticancer drug doxorubicin onto NGO functionalized with antibody for selective killing of cancer cells *in vitro*.[162]

Compared with fluorescent carbon dots, GQDs can be used for two-photon or multi-photon luminescence imaging.[163, 164] Qian *et al.* used PEGylated graphene oxide nanoparticles to label HeLa cells,[163] and observed that graphene oxide nanoparticles were mainly localized in the mitochondria, endoplasmic reticulum, Golgi apparatus, and lysosomes of HeLa cells with a two-photon scanning microscope. They intravenously injected graphene oxide nanoparticles into mouse bodies from the tail vein, and observed their flow, distribution, and clearance in the blood vessels, utilizing a deep-penetrating two-photon imaging technique. These nanoparticles were also injected into the brains of gene transfected mice, and the *in vivo* two-photon luminescence imaging results showed that graphene oxide nanoparticles were located at 300 μm depth in the brain,

demonstrating the advantage of QGDs for deep imaging in tissues. Recently, Liu *et al.* prepared nitrogen-doped GQDs as efficient two-photon fluorescent probes.[164] These N-GQDs exhibited the highest two-photon absorption cross-section (up to 48000 Göppert-Mayer units) among the carbon-based materials. They also demonstrated a large imaging depth of 1800 μm by a study of penetration depth in tissue phantom (Figure 16).

In summary, surface-modified fluorescent carbon nanomaterials (carbon dots and GQDs) have small size, distinctive photoluminescence properties, low toxicity, and low cost. These advantages offer them great potential for optical imaging and biomedical applications, as they might gradually replace conventional semiconductor QDs in these aspects.

5 Ultra-small up-conversion nanocrystals

Compared with previously mentioned fluorescent nanomaterials, up-conversion nanostructures, especially lanthanide-doped nanocrystals, have distinct advantages in fluorescence bioimaging, such as low autofluorescence background, large anti-Stokes shifts, sharp emission bandwidth, high resistance to photobleaching, and high penetration depth and temporal resolution,[165-171] In addition, they can be used for multimodal bioimaging and therapy (Figure 17). More bioapplications of up-conversion nanoparticles can be found in recent reviews.[165, 169-171] However, they usually have a larger size in comparison with those nanoprobes described previously (i.e. QDs, metal nanoclusters, carbon dots, and GQDs). There are few reports on ultra-small up-conversion nanoparticles, especially those below 5 nm.[172-177] Herein we mainly introduce the fundamentals of up-conversion nanoparticles and the progress in preparation and imaging application of ultra-small nanoparticles.

For up-conversion nanocrystals, their emission process involves the sequential absorption of two or more photons, which is fundamentally different from the multi-photon process, where the absorption of photons takes place simultaneously. There are three types of up-conversion mechanisms, i.e. excited state absorption (ESA), energy transfer up-conversion (ETU), and photon avalanche.[166] The up-conversion nanocrystals usually consist of activators, sensitizers, and the host matrix [Figure 17(a)]. The activators should have more excited energy levels, and the energy difference between each excited level and the ground level should be close enough to facilitate photon absorption and energy transfer in the up-conversion process. Lanthanide ions such as Er^{3+}, Tm^{3+}, and Ho^{3+} have such ladder-like energy levels and are usually selected as activators. In order to improve the luminescence efficiency, sensitizers are introduced. Yb^{3+} is usually chosen as sensitizer because it has only one excited energy level ($^2F_{5/2}$), and the transition between the ground level ($^2F_{7/2}$) and excited level is strongly resonant with many f-f transitions of lanthanide ions. The concentration of activators, and the molar ratio between activators and sensitizers is usually kept low to avoid the quenching effect.[166] Zhao *et al.*, however, showed that up-conversion luminescence can be significantly enhanced by using much higher activator concentrations (e.g. 8 mol% Tm^{3+} in $NaYF_4$) under relatively high-irradiance excitation.[178] The authors attributed the high brightness to a combination of high excitation intensity, increased
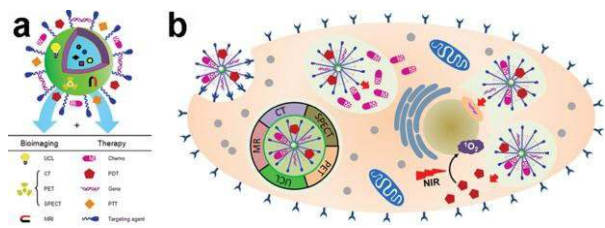

Figure 17. (a) Schematic structure of multifunctional up-conversion nanoparticles; and **(b)** their potential applications in bioimaging and therapy. Reproduced from Ref. 165.

activator concentration, and accelerated sensitizer-activator energy transfer rate arising from the decreased average minimum distance between adjacent lanthanide ions. The high brightness makes it possible to remotely track a single nanocrystal with a microstructured optical-fibre dip sensor.[178]

Ideal host materials should have low lattice phonon energy and the minimum lattice mismatch with dopants (activators and sensitizers). Rare-earth fluorides are generally chosen as host materials, as rare-earth ions have similar ionic size and chemical properties to lanthanide ions, and their fluorides exhibit low phonon energy and high chemical stability.[166] In particular, $NaGdF_4$ is extensively used as it can serve as a positive contrast agent for magnetic resonance imaging (MRI). Johnson *et al.* prepared four different sizes of β-$NaGdF_4$ nanoparticles between 2.5 nm and 8.0 nm.[172] They found that the longitudinal relaxivity of nanoparticles increased from 3.0 $mM^{-1}s^{-1}$ to 7.2 $mM^{-1}s^{-1}$ with decreasing particle size from 8.0 nm to 2.5 nm. The authors doped Yb^{3+} and Tm^{3+} into β-$NaGdF_4$ to form 3.5 nm particles, which exhibited an emission at 800 nm under the excitation of a 980-nm laser.[172] Their results highlight the importance of preparation of ultra-small nanoparticles in order to achieve large relaxivity for MRI.

The fluorescence of up-conversion nanoparticles can be engineered through modulation of activators, sensitizers, host materials, and their crystal phase, particle size, and surface coating. Hasse and co-workers demonstrated the first example of multicolour emission of Yb^{3+}/Er^{3+}, and Yb^{3+}/Tm^{3+} co-doped α-$NaYF_4$ colloidal solution.[179] In 2008, Wang *et al.* developed a general and versatile approach to fine-tune the multicolour emissions over a broad range with single wavelength excitation.[180] By introducing Gd^{3+} during preparation, the authors simultaneously controlled the crystal phase, particle size, and optical properties of the resultant nanocrystals.[181] Recently, a core-shell structure with a set of lanthanide ions incorporated into separated layers was designed. The core-shell structure can minimize the deleterious effects of cross-relaxation. The bright up-conversion emission was achieved through Gd^{3+} mediated energy migration without long-lived intermediate energy states.[182, 183]

In up-conversion nanoparticles, minimizing the depletion of excitation energy is the key to tuning their luminescence. The excitation energy can randomly migrate from an atom to its neighbouring atoms that are isotropically distributed in a 3D structured crystal sublattice (type I in Figure 18). This energy can also migrate in a crystal with a 2D layer structure (type II), or in a crystal featuring a 1D atomic chain structure (type III).[184]
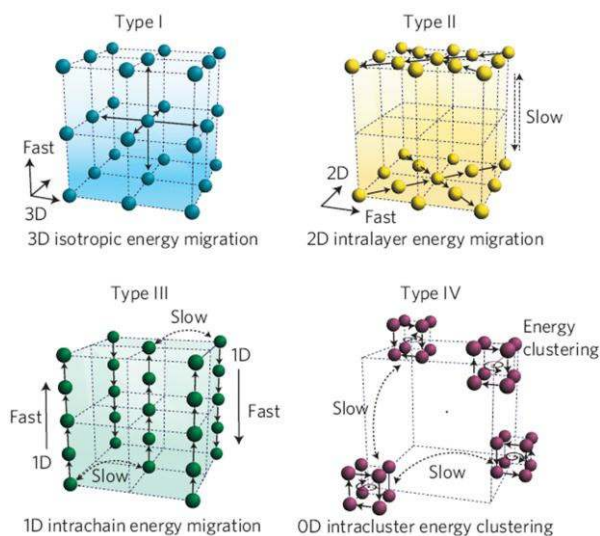
Figure 18. Schematic illustration of the topological energy migration pathways in different types of crystal sublattice. Reproduced from Ref. 184.
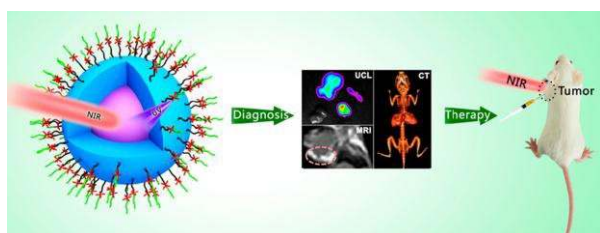

Figure 19. Multifunctional upconversion nanoparticles for diagnosis and treatment of cancer through imaging-guided therapy. Reproduced from Ref. 186.

Recently, Wang *et al.* proposed that migration of the excitation energy can be effectively minimized through use of a type IV (Figure 18) lattice containing arrays of isolated atomic clusters.[184] This allows to minimize the concentration quenching of the luminescence, and generates an unusual four-photon-promoted violet up-conversion emission from KYb_2F_7:Er (2 mol%) with an intensity more than eight times higher than that previously reported.[184] The approach of enhancing up-conversion through energy clustering at the sublattice level may provide new opportunities to engineer up-conversion nanoparticles for diverse applications.

The good understanding of the energy migration, luminescence mechanism, and the recent advances in wet chemistry have enabled the fine-tuning of particle size (even in the small size range), crystal structure, surface functionalities, and optical properties of up-conversion nanocrystals for bioimaging, drug delivery, and sensing.[165, 167, 169] Their fluorescence has been applied to image cells and small animals.[185] As mentioned previously, Gd-based up-conversion nanoparticles are particularly interesting as they can serve as fluorescent nanoprobes and contrast agents of MRI simultaneously. Recently, a multifunctional drug delivery system combining up-conversion luminescence/magnetic resonance/computer tomography trimodality imaging and NIR-activated platinum pro-drug delivery has been developed by Dai and co-workers (Figure 19).[186]   Organic-soluble   core−shell
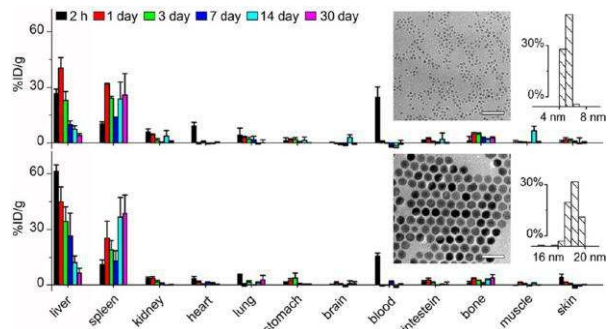

Figure 20. Biodistribution of 5.1nm (NaGdF4) and 18.5nm (NaGdF4:Yb,Er) nanoparticles in different organs and tissues of mice. Reproduced from Ref. 189.

$NaYF_4:Yb^{3+}/Tm^{3+}@NaGdF_4:Yb^{3+}$ nanoparticles were first prepared by complex thermal decomposition method, followed by surface modification and conjugation with the trans-platinum (IV) pro-drug. The up-conversion nanoparticles can not only deliver the platinum (IV) pro-drugs into the cells effectively, but convert near-infrared light into UV to activate pro-drug as well. Meanwhile, they can further serve as contrast agents for multimodality imaging to guide cancer treatment. The pro-drug-conjugated nanoparticles under near-infrared irradiation led to better inhibition of tumor growth than that under direct UV irradiation in the mouse test.[186] Such multifunctional up-conversion nanoparticles have been a subject of intensive research due to their potential in disease diagnosis and treatment.[165, 170]

For *in-vivo* bioapplications, one of the major issues for up-conversion nanocrystals is the fate of nanoparticles and potential toxicity of lanthanide ions.[187, 188] Liu *et al.* prepared 5.1 nm $NaGdF_4$ and 18.5 nm $NaGdF_4$:Yb/Er nanoparticles with the same surface modification and investigated their biodistributions in different organs and tissues of mice (Figure 20).[189] The accumulation of both types of nanoparticles in liver decreased with the circulation time. In contrast, their accumulation in spleen increased with the circulation time. This suggests that both of these nanoparticles may be eliminated through the biliary pathway. Analysis of urine collected at different time points indicates that renal clearance was one of the major elimination pathways for 5.1-nm particles, but not for 18.5-nm particles. Further analysis on faces by TEM shows that these particles do not change in shape and size, suggesting the high stability of up-conversion nanoparticles *in vivo*.[189]

Although up-conversion nanoparticles do not show acute toxicity at the cell or animal level, it is necessary to investigate their long-term toxicity. Another drawback of up-conversion nanocrystals is the low quantum yield (usually less than 1%) in comparison with other fluorescent agents.[165] Preparation of highly efficient up-conversion nanocrystals remains a great challenge.

6 Fluorescent silicon nanoparticles

Fluorescent silicon nanoparticles (Si NPs) have also attracted considerable attention in bioapplications due to their excellent biocompatibility as silicon naturally exists in human body as a
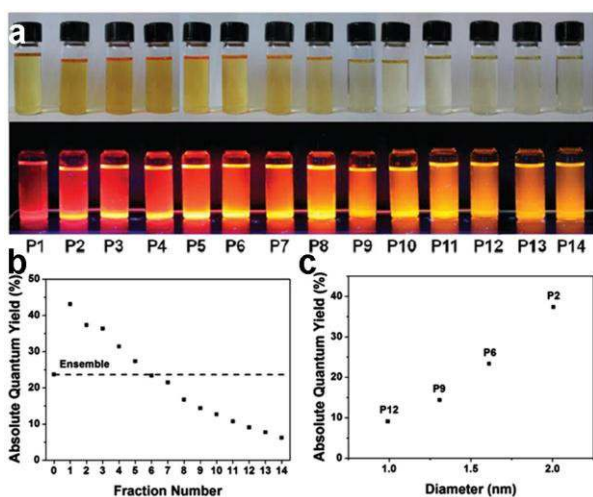
Figure 21. (a) Silicon nanoparticle fractions under ambient light and under photoexcitation at 365 nm; **(b-c)** size-dependent absolute QYs of Si nanoparticles. Reproduced from Ref. 191.

trace element.[18, 20, 190] More importantly, they have tunable fluorescence from visible to near-infrared window. Compared with other semiconducting QDs, the preparation of high-quality water-soluble and biocompatible Si QDs is devious and laborious. Colloidal Si NPs are conventionally prepared by etching annealed SiO_x with HF, plasma approach, electrochemical method, laser ablation, reduction of $SiCl_4$, and solvothermal reaction of sodium silicide with NH_4Br.[18, 190-193] These Si NPs are usually functionalized with hydrophobic ligands such as styrene, alkyl, and octene. They are photochemically stable in non-polar solvents up to 1 year.[192] For example, high-temperature thermal processing of the sol-gel precursor derived from trichlorosilane ($HSiCl_3$) produced Si NPs embedded within the SiO_2 matrix.[191, 194] Si NPs were released after etching the SiO_2 matrix with HF, and then passivated with allylbenzene through the thermally initiated hydrosilylation reaction. The resultant colloidal Si NPs were fractionated by size selective precipitation to obtain monodisperse nanoparticles, which showed strong quantum confinement effects and size-dependent absolute QYs (Figure 21).[191] The absolute QYs increased with particle size up to 43%.

During preparation, Si NPs can be chemically doped to introduce other functions.[195, 196] Paramagnetic fluorescent Si NPs were prepared by solvothermal decomposition of Mn-doped sodium silicide.[195] The resultant Mn-doped Si NPs showed a longitudinal relaxivity (r_1) of 25.50 ± 1.44 $mM^{-1}s^{-1}$ and a transverse relaxivity (r_2) of 89.01 ± 3.26 $mM^{-1}s^{-1}$ under a magnetic field of 1.4 T at 37 °C. Similarly, Fe-doped Si NPs were prepared and exploited as bimodal imaging agents.[196] The use of reactive sodium silicide makes their control preparation difficult and could limit their broad applications, and thus development of novel preparation approaches is necessary.

Similar to carbon dots and GQDs, Si NPs produced from different methods seem identical, but their optical properties are dramatically different. For example, the Si NPs prepared with high-temperature method routinely exhibit photoluminescence agreeing with the effective mass approximation (EMA), while those prepared via solution methods exhibit blue emission
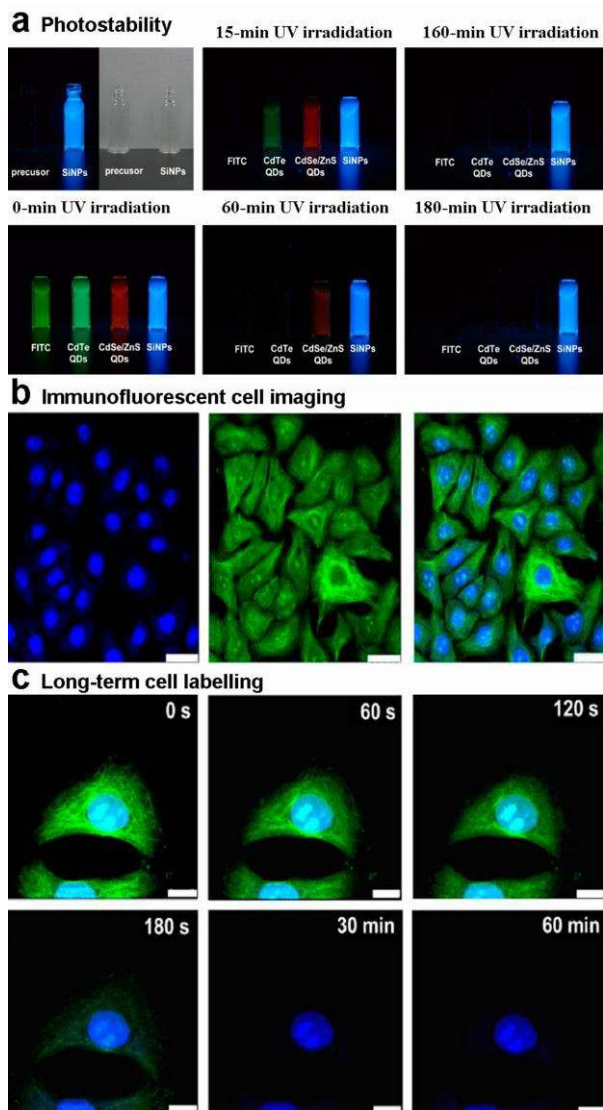

Figure 22. (a) Photostability of Si NPs in comparison with FITC, CdTe QDs and CdSe/ZnS QDs; **(b)** cell nuclei are labeled by Si NPs (Left), microtubules are labeled by FITC (middle); and superposition of the two fluorescence images (right); **(c)** time-dependent stability comparison of fluorescence signals of Hela cells labeled by Si NPs (blue) and FITC (green). Reproduced from Ref. 204.

somewhat independent of particle size.[197, 198] Recently, Dasog *et al.* prepared Si NPs using three most widely cited procedures (i.e. etching of annealed SiO_x, reduction of $SiCl_4$, and solvothermal reaction of sodium silicide with NH_4Br),[197] and found their conversion of red-fluorescence to blue emission. Their findings suggest that the presence of trace nitrogen and oxygen even at the ppm level in Si NPs gives rise to the blue emission, and support the hypothesis that the nitrogen defect or impurity site contributes to the blue emission.[197]

In order to apply Si NPs to bioimaging, tremendous efforts have been made to prepare water-soluble and biocompatible Si NPs through simple and efficient methods.[199-205] For example, Si NPs with excellent aqueous dispersibility, robust photo- and pH-stability, strong fluorescence (~15%), and favorable size (~4 nm) are facilely and rapidly prepared from Si nanowires and glutaric

acid in a short reaction time (e.g., 15 min) by He and co-workers.[202] These Si NPs are particularly suitable for long-term and real-time cellular imaging due to their higher photostability than II-VI QDs and dyes (e.g. CdTe QDs and FITC). Distinctive red fluorescence of Si NPs can be retained throughout 240-min irradiation. In contrast, the green fluorescence of FITC rapidly diminishes in 3 min due to severe photo bleaching, and the red signals of CdTe QDs nearly vanishes after 25-min irradiation. The MTT assays showed negligible cellular toxicity to HeLa cells, demonstrating the excellent biocompatibility of Si NPs. Furthering their research, the authors used (3-aminopropyl)trimethoxylsiliane as precursor and prepared 2.2 nm Si NPs by the similar method.[204] The obtained Si NPs exhibited strong green fluorescence with a QY of 20-25%, biocompatibility, and robust photo- and pH-stability. As shown in Figure 22, FITC, CdTe and CdSe/ZnS QDs, and Si NPs exhibited distinct fluorescence behaviors during initial UV irradiation.[204] The fluorescent signals of the former three samples were gradually reduced with increasing irradiation time. The fluorescence of FITC was completely quenched within 15 min irradiation. In contrast, the Si NPs preserved stable and bright fluorescence during long-time (e.g., 180 min) irradiation under the same conditions. Figure 22c also shows that Si NPs-labelled nuclei (blue) and the FITC-labelled cellular microtubules (green) were intense and clearly spectrally resolved, respectively. The Si NP-labelled nuclei retained stable fluorescence during observation for 60 min, however the fluorescence from FITC labels drastically decreased in 3 min due to severe photo bleaching.

In addition to *in vitro* labelling cells, Si NPs can also be used in multiple cancer-related *in vivo* applications, including tumor vasculature targeting, sentinel lymph node mapping, and multicolor NIR imaging in live mice.[206] Erogbogbo and coworkers demonstrated that Si NPs can overcome dispersibility and functionalization challenges for *in vivo* imaging through surface functionalization, PEGylated micelle encapsulation, and bioconjugation process, which produced bright, targeted nanospheres with stable luminescence and long (>40 h) tumor accumulation time *in vivo*. Recently, the biodistribution and toxicity of Si NPs in mice and monkeys have been assessed (Figure 23).[207] The top images in Figure 23 show the biodistribution of Si NPs in mice, the fluorescence image of frozen tissue sections, and the confocal images, which clearly reveals particles localized in the liver, spleen, and kidneys after injection. The ICP-MS data show notable increase of silicon levels in the liver, spleen, lung, kidneys, and lymph. The concentration of silicon in the lymph and kidneys declined over the 14-week time period, while the liver and spleen retained a significant fraction of the silicon injected, even after 14 weeks.[207] There is no evidence of the biodegradability of silicon NPs. The bottom images in Figure 23 display the histological images of the brain, cerebellum, atrium, ventricle, heart muscle, lung, kidney, liver, spleen, renal tubule, intestine, lymph nodes, and skin of the rhesus macaques.[207] There was no sign of nanoparticle-induced changes in these organs and tissues. This research indicates neither mice nor monkeys showed overt signs of toxicity reflected in their behavior, body mass, or blood chemistry. The biodistribution of Si NPs in mice was also quantitatively
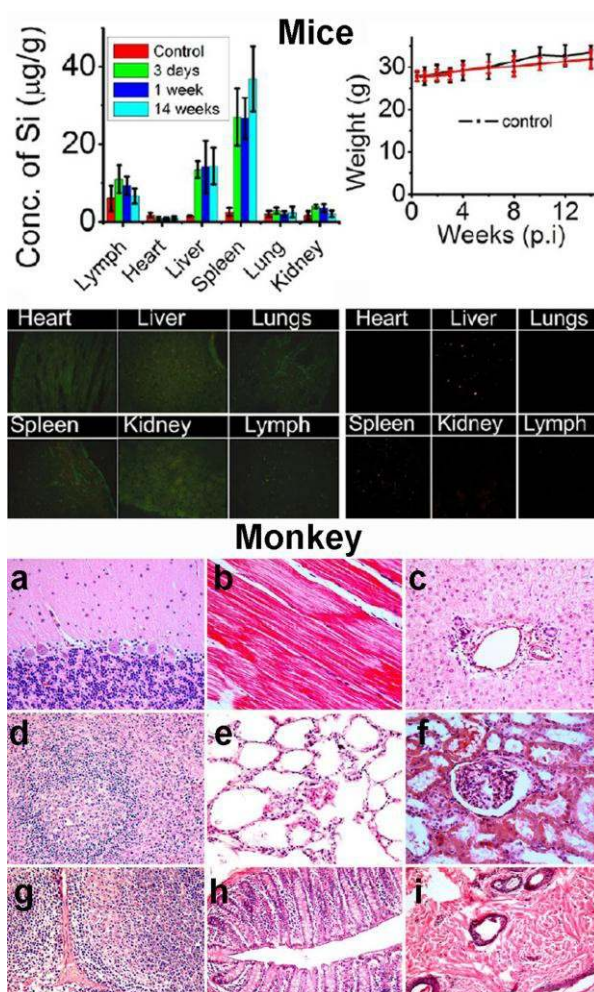

Figure 23. (Top) biodistributions of Si NPs in mice assessed by ICP-MS analysis, fluorescence images of frozen tissue sections, confocal microscopy images; **(bottom)** histological images of (a) brain, (b) heart, (c) liver, (d) spleen, (e) lung, (f) kidney, (g) lymph, (h) intestine, and (i) skin harvested from rhesus macaques administrated with Si NPs. Reproduced from Ref. 207.

evaluated by *in vivo* positron emission tomography (PET) imaging and *ex vivo* gamma counting.[208] A new macrocyclic ligand-^{64}Cu^{2+} complex was conjugated with dextran-coated Si NPs and served as PET agent. The results show that conjugates were excreted via renal filtration shortly post injection and also accumulated in the liver, again demonstrating the stability and biocompatibility of Si NPs.

In summary, Si NPs have tuneable fluorescence from visible to near-infrared window, excellent biocompatibility, chemical, and photostability. These properties make them very attractive in bioimaging, however long-term studies on their safety and adverse effects are still needed for their clinical applications.

7 Summary and outlook

We have summarized the current state of the art on ultra-small inorganic nanoparticles for fluorescence bioimaging. These ultra-small nanoparticles bridge the gap between big particles and molecules. They have unique properties and great potential in

molecular imaging for diagnosis and treatment of cancer and other diseases, as they could escape from macrophages, pass biological barriers, and be easily degraded or excreted in comparison with large particles.

The ultra-small fluorescent probes we addressed include the conventional QDs, fluorescent metal nanoclusters, carbon-based nanomaterials, up-conversion nanocrystals, and silicon nanoparticles. The fluorescence mechanisms in metal nanoclusters, carbon dots, and graphene quantum dots are not completely clear as yet. Although they can be prepared by various wet chemistry methods, it remains a challenge to prepare robust fluorescent probes with high photostability (i.e. non-blinking), chemical stability, high quantum yield, and tunable emissions in the visible to NIR window. From the applications perspective, some of them face the issue of toxicity, especially semiconducting QDs and up-conversion nanocrystals, as they have toxic elements such as cadmium and lanthanides. Various approaches and coatings have been developed to modify and functionalize their surfaces to overcome these shortcomings. In addition to the issues of fluorescent nanoprobes themselves, there are some important issues that have to be considered for practical applications, including their interactions with proteins and other biomolecules, their interactions with cells, their endocytosis and intracellular stability and behaviour, and their metabolism and excretion. These issues have not been well understood, despite some progresses on bio-interface interactions in the biological environments have been made in recent years.[61-63]

The use of fluorescence imaging alone could lead to inaccurate diagnosis or misdiagnosis, due to the low spatial and temporal resolution, and the sensitivity of fluorescence to external environments. Simultaneous use of multi-modal imaging (e.g. magneto-fluorescence) could overcome the disadvantages of individual methods. There are increasing reports on the combination of fluorescence with other imaging methods such as MRI, CT, and PET.[60, 209-212] There are few commercial multifunctional instruments for multimodal imaging, however. Relocating biological samples between different imaging instruments could lead to inaccuracy.[213] Development of multimodal imaging that employs a single instrument is an attractive solution.[213] In addition, incorporation of therapeutics into multimodal nano-agents for early detection and treatment will be an important feature of future nanotheranostics.

Notes and references

a Institute of Superconducting & Electronic Materials, The University of Wollongong, NSW 2500, Australia. Fax: +61-2-42215731; E-mail: zhenl@uow.edu.au
b Australian Institute for Bioengineering and Nanotechnology, The University of Queensland, Queensland 4072, Australia. Fax: +61-7-33463973; E-mail: gordonxu@uq.edu.au
c School of Chemistry and Chemical Engineering, Huazhong University of Science and Technology, Wuhan, 430074, China.

1. P. Alivisatos, *Science*, 1996, **271**, 933-937.

2. Z. Li, Q. Sun and M. Y. Gao, *Angew. Chem. Int. Ed.*, 2005, **44**, 123-126.

3. M. F. Yu, O. Lourie, M. J. Dyer, K. Moloni, T. F. Kelly and R. S. Ruoff, *Science*, 2000, **287**, 637-640.

4. A. K. Geim and K. S. Novoselov, *Nat. Mater.*, 2007, **6**, 183-191.

5. K. N. Shinde, S. J. Dhoble, H. C. Swart and K. Park, eds., *Phosphate Phosphors for Solid-State Lighting*, Springer-Verlag, Berlin, 2012.

6. B. N. G. Giepmans, S. R. Adams, M. H. Ellisman and R. Y. Tsien, *Science*, 2006, **312**, 217-224.

7. R. Weissleder and M. J. Pittet, *Nature*, 2008, **452**, 580-589.

8. A. Policard, *C R Séances Soc Biol Fil.*, 1924, **91**, 1423-1424.

9. P. Alivisatos, *Nat. Biotechnol.*, 2004, **22**, 47-52.

10. X. Michalet, F. F. Pinaud, L. A. Bentolila, J. M. Tsay, S. Doose, J. J. Li, G. Sundaresan, A. M. Wu, S. S. Gambhir and S. Weiss, *Science*, 2005, **307**, 538-544.

11. I. L. Medintz, H. T. Uyeda, E. R. Goldman and H. Mattoussi, *Nat. Mater.*, 2005, **4**, 435-446.

12. V. Biju, T. Itoh and M. Ishikawa, *Chem. Soc. Rev.* , 2010, **39**, 3031-3056.

13. H. Koo, M. S. Huh, J. H. Ryu, D. E. Lee, I. C. Sun, K. Choi, K. Kim and I. C. Kwon, *Nano Today*, 2011, **6**, 204-220.

14. I. L. Medintz, M. H. Stewart, S. A. Trammell, K. Susumu, J. B. Delehanty, B. C. Mei, J. S. Melinger, J. B. Blanco-Canosa, P. E. Dawson and H. Mattoussi, *Nat. Mater.*, 2010, **9**, 676-684.

15. L. Shang, F. Stockmar, N. Azadfar and G. U. Nienhaus, *Angew. Chem. Int. Ed.*, 2013, **52**, 11154-11157.

16. A. W. Zhu, Q. Qu, X. L. Shao, B. Kong and Y. Tian, *Angew. Chem. Int. Ed.*, 2012, **51**, 7185-7189.

17. P. G. Luo, S. Sahu, S.-T. Yang, S. K. Sonkar, J. Wang, H. Wang, G. E. LeCroy, L. Cao and Y.-P. Sun, *J. Mater. Chem. B*, 2013, **1**, 2116-2127.

18. M. L. Mastronardi, E. J. Henderson, D. P. Puzzo and G. A. Ozin, *Adv. Mater.*, 2012, **24**, 5890-5898.

19. D. D. V. II and R. E. Schaak, *Chem. Soc. Rev.*, 2013, **42**, 2861-2879.

20. F. Peng, Y. Y. Su, Y. L. Zhong, C. Fan, S.-T. Lee and Y. He, *Acc. Chem. Res.*, 2014, **47**, 10.1021/ar400221g.

21. P. M. Allen and M. G. Bawendi, *J. Am. Chem. Soc.*, 2008, **130**, 9240-9241.

22. H. Z. Zhong, Z. L. Bai and B. S. Zou, *J. Phys. Chem. Lett.*, 2012, **3**, 3167-3175.

23. S. L. Shen and Q. B. Wang, *Chem. Mater.*, 2013, **25**, 1166-1178.

24. C. B. Murray, D. J. Norris and M. G. Bawendi, *J. Am. Chem. Soc.*, 1993, **115**, 8706-8715.

25. Y. Yin and A. P. Alivisatos, *Nature*, 2005, **437**, 664-670.

26. Z. A. Peng and X. G. Peng, *J. Am. Chem. Soc.*, 2001, **123**, 183-184.

27. D. V. Talapin, A. L. Rogach, A. Kornowski, M. Haase and H. Weller, *Nano Lett.*, 2001, **1** 207-211.

28. Z. A. Peng and X. G. Peng, *J. Am. Chem. Soc.*, 2002, **124**, 3343-3353.

29. X. G. Peng, L. Manna, W. D. Yang, J. Wickham, E. Scher, A. Kadavanich and A. P. Alivisatos, *Nature*, 2000, **404**, 59-61.

30. X. G. Peng, *Adv. Mater.*, 2003, **15**, 459-463.

31. D. J. Milliron, S. M. Hughes, Y. Cui, L. Manna, J. B. Li, L. W. Wang and A. P. Alivisatos, *Nature*, 2004, **430**, 190-195.

32. X. Peng, J. Wickham and A. P. Alivisatos, *J. Am. Chem. Soc.*, 1998, **120**, 5343-5344.

33. L. H. Qu and X. G. Peng, *J. Am. Chem. Soc.*, 2002, **124**, 2049-2055.

34. J. J. Li, Y. A. Wang, W. Z. Guo, J. C. Keay, T. D. Mishima, M. B. Johnson and X. G. Peng, *J. Am. Chem. Soc.*, 2003, **125**, 12567-12575.

35. R. G. Xie, U. Kolb, J. X. Li, T. Basche and A. Mews, *J. Am. Chem. Soc.*, 2005, **127**, 7480-7488.

36. O. Chen, J. Zhao, V. P. Chauhan, J. Cui, C. Wong, D. K. Harris, H. Wei, H.-S. Han, D. Fukumura, R. K. Jain and M. G. Bawendi, *Nat. Mater.*, 2013, **12**, 445-451.

37. H. Y. Qin, Y. Niu, R. Y. Meng, X. Lin, R. C. Lai, W. Fang and X. G. Peng, *J. Am. Chem. Soc.*, 2014, **136**, 179-187.

38. X. Y. Wang, X. F. Ren, K. Kahen, M. A. Hahn, M. Rajeswaran, S. Maccagnano-Zacher, J. Silcox, G. E. Cragg, A. L. Efros and T. D. Krauss, *Nature*, 2009, **459**, 686-689.

39. Z. Li, Q. Sun, Z. Zhu, S. C. Smith and G. Q. M. Lu, in *One-Dimensional Nanostructures: Principles and Applications*, eds. T. Y. Zhai and J. N. Yao, Wiley, 2013, pp. 65-102.

40. Z. Li, L. N. Cheng, Q. Sun, Z. H. Zhu, M. J. Riley, M. Aljada, Z. X. Cheng, X. L. Wang, G. R. Hanson, S. Z. Qiao, S. C. Smith and G. Q. Lu, *Angew. Chem. Int. Ed.*, 2010, **49**, 2777-2781.

41. Z. Li, A. Kornowski, A. Myalitsin and A. Mews, *Small*, 2008, **4**, 1698-1702.

42. Z. Li, Ö. Kurtulus, F. Nan, A. Myalitsin, Z. Wang, A. Kornowski, U. Pietsch and A. Mews, *Adv. Funct. Mater.*, 2009, **19**, 3650-3661.

43. Z. Wang, Z. Li, A. Kornowski, X. D. Ma, A. Myalitsin and A. Mews, *Small*, 2011, **7**, 2464-2468.

44. N. Fu, Z. Li, A. Myalitsin, M. Scolari, R. T. Weitz, M. Burghard and A. Mews, *Small*, 2010, **6**, 376-380.

45. Z. Li, A. J. Du, Q. Sun, M. Aljada, L. N. Cheng, Z. H. Zhu, M. J. Riley, Z. X. Cheng, X. L. Wang, J. Hall, E. Krausz, S. Z. Qiao, S. C. Smith and G. Q. Lu, *Chem. Commun.*, 2011, **47**, 11894-11896.

46. A. Myalitsin, C. Strelow, Z. Wang, Z. Li, T. Kipp and A. Mews, *ACS Nano*, 2011, **5**, 7920-7927.

47. Z. Li, A. J. Du, Q. Sun, M. Aljada, Z. H. Zhu and G. Q. Lu, *Nanoscale*, 2012, **4**, 1263-1266.

48. Z. Li, Q. Sun, X. D. Yao, Z. H. Zhu and G. Q. M. Lu, *J. Mater. Chem.*, 2012, **22**, 22821-22831.

49. C. Han, Z. Li and S. X. Dou, *Chin. Sci. Bulletin*, 2014, In press.

50. O. Kurtulus, Z. Li, A. Mews and U. Pietsch, *Phys. Stat. Sol. A*, 2009, **206**, 1752-1756.

51. K. P. Kandel, U. Pietsch, Z. Li and O. Kurtulus, *Phys. Chem. Chem. Phys.*, 2013, **15**, 4444-4450.

52. Z. Li, X. Ma, Q. Sun, Z. Wang, J. Liu, Z. Zhu, S. Z. Qiao, S. C. Smith, G. M. Lu and A. Mews, *Eur. J. Inorg. Chem.*, 2010, **27**, 4325-4331.

53. A. Henglein, *Ber. Bunsen-Ges. Phys. Chem.*, 1982, **86**, 301-305.

54. U. Resch, H. Weller and A. Henglein, *Langmuir*, 1989, **5**, 1015-1020.

55. A. L. Rogach, L. Katsikas, A. Kornowski, I. G. Popovic, D. Su, A. Eychmuller and H. Weller, *Ber. Bunsen-Ges. Phys. Chem.*, 1996, **100**, 1772-1778.

56. Y. L. Li, L. H. Jing, R. R. Qiao and M. Y. Gao, *Chem. Comm.*, 2011, **47**, 9293-9311.

57. H. B. Bao, Y. J. Gong, Z. Li and M. Y. Gao, *Chem. Mater.*, 2004, **16**, 3853-3859.

58. Y. Zhu, Z. Li, M. Chen, H. M. Cooper, G. Q. Lu and Z. P. Xu, *J. Colloid Interface Sci.*, 2013, **390**, 3-10.

59. S. R. Sturzenbaum, M. Hockner, A. Panneerselvam, J. Levitt, J. S. Bouillard, S. Taniguchi, L. A. Dailey, R. A. Khanbeigi, E. V. Rosca, M. Thanou, K. Suhling, A. V. Zayats and M. Green, *Nat. Nanotechnol.*, 2013, **8**, 57-60.

60. Y. A. Zhu, H. Hong, Z. P. Xu, Z. Li and W. B. Cai, *Curr. Mol. Med.*, 2013, **13**, 1549-1567.

61. L. C. Cheng, X. M. Jiang, J. Wang, C. Y. Chen and R. S. Liu, *Nanoscale*, 2013, **5**, 3547-3569.

62. L. Shang and G. U. Nienhaus, *Mater. Today*, 2013, **16**, 58-66.

63. Y. C. Wang, R. Hu, G. M. Lin, I. Roy and K. T. Yong, *ACS Appl. Mater. Interfaces*, 2013, **5**, 2786-2799.

64. W. C. W. Chan and S. M. Nie, *Science*, 1998, **281**, 2016-2018.

65. C. X. C. Lin, Z. Li, S. Brumbley, L. Petrasovits, R. McQualter, C. Yu and G. Q. M. Lu, *J. Mater. Chem.*, 2011, **21**, 7565-7571.

66. A. M. Derfus, W. C. W. Chan and S. N. Bhatia, *Nano Lett.*, 2004, **4**, 11-18.

67. M. Bruchez, M. Moronne, P. Gin, S. Weiss and A. P. Alivisatos, *Science*, 1998, **281**, 2013-2016.

68. W. Stöber and A. Fink, *J Colloid Interf Sci.*, 1968, **26**, 62-29.

69. Y. H. Yang and M. Y. Gao, *Adv. Mater.*, 2005, **17**, 2354-2357.

70. T. Nann and P. Mulvaney, *Angew. Chem. Int. Ed.*, 2004, **43**, 5393-5396.

71. L. Jing, C. Yang, R. Qiao, M. Niu, M. Du, D. Wang and M. Gao, *Chem. Mater.*, 2010, **22**, 420-427.

72. Y. Zhu, Z. Li, M. Chen, H. M. Cooper, G. Q. Lu and Z. P. Xu, *Chem. Mater.*, 2012, **24**, 421-423.

73. W. Jiang, B. Y. S. Kim, J. T. Rutka and W. C. W. Chan, *Nat. Nanotechnol.*, 2008, **3**, 145-150.

74. Y. Zhu, Z. Li, M. Chen, H. M. Cooper and Z. P. Xu, *J. Mater. Chem. B*, 2013, **1**, 2315-2323.

75. Z. L. Cheng, A. Al Zaki, J. Z. Hui, V. R. Muzykantov and A. Tsourkas, *Science*, 2012, **338**, 903-910.

76. X. H. Gao, Y. Y. Cui, R. M. Levenson, L. W. K. Chung and S. M. Nie, *Nat. Biotechnol.*, 2004, **22**, 969-976.

77. E. I. Sega and P. S. Low, *Cancer Metast Rev*, 2008, **27**, 655-664.

78. B. Xue, D. W. Deng, J. Cao, F. Liu, X. Li, W. Akers, S. Achilefu and Y. Q. Gu, *Dalton T*, 2012, **41**, 4935-4947.

79. D. A. Ossipov, *Expert opinion on drug delivery*, 2010, **7**, 681-703.

80. S. H. Bhang, N. Won, T. J. Lee, H. Jin, J. Nam, J. Park, H. Chung, H. S. Park, Y. E. Sung, S. K. Hahn, B. S. Kim and S. Kim, *Acs Nano*, 2009, **3**, 1389-1398.

81. K. Bourzac, *Nature*, 2013, **493**, 283-283.

82. R. Hardman, *Environ. Health Perspect.*, 2006, **114**, 165-172.

83. H. S. Choi, W. Liu, P. Misra, E. Tanaka, J. P. Zimmer, B. I. Ipe, M. G. Bawendi and J. V. Frangioni, *Nat. Biotechnol.*, 2007, **25**, 1165-1170.

84. H. S. Choi, W. H. Liu, F. B. Liu, K. Nasr, P. Misra, M. G. Bawendi and J. V. Frangioni, *Nat. Nanotechnol.*, 2010, **5**, 42-47.

85. L. Ye, K. T. Yong, L. W. Liu, I. Roy, R. Hu, J. Zhu, H. X. Cai, W. C. Law, J. W. Liu, K. Wang, J. Liu, Y. Q. Liu, Y. Z. Hu, X. H. Zhang, M. T. Swihart and P. N. Prasad, *Nat. Nanotechnol.*, 2012, **7**, 453-458.

86. S. Link and M. A. El-Sayed, *Annu. Rev. Phys. Chem.*, 2003, **54**, 331-366.

87. L. Shang, S. J. Dong and G. U. Nienhaus, *Nano Today*, 2011, **6**, 401-418.

88. Y. Z. Lu and W. Chen, *Chem. Soc. Rev.*, 2012, **41**, 3594-3623.

89. S. Choi, R. M. Dickson and J. H. Yu, *Chem. Soc. Rev.*, 2012, **41**, 1867-1891.

90. Y. H. Li, J. Xing, Z. J. Chen, Z. Li, F. Tian, L. R. Zheng, H. F. Wang, P. Hu, H. J. Zhao and H. G. Yang, *Nat. Commun.*, 2013, **4**.

91. H. F. Qian, M. Z. Zhu, Z. K. Wu and R. C. Jin, *Acc. Chem. Res.*, 2012, **45**, 1470-1479.

92. A. Mooradian, *Phys. Rev. Lett.*, 1969, **22**, 185-187.

93. J. P. Wilcoxon, J. E. Martin, F. Parsapour, B. Wiedenman and D. F. Kelley, *J. Chem. Phys.*, 1998, **108**, 9137-9143.

94. J. Zheng, J. T. Petty and R. M. Dickson, *J. Am. Chem. Soc.*, 2003, **125**, 7780-7781.

95. J. Zheng, C. W. Zhang and R. M. Dickson, *Phys. Rev. Lett.*, 2004, **93**, 077402.

96. J. Zheng, P. R. Nicovich and R. M. Dickson, *Annu. Rev. Phys. Chem.*, 2007, **58**, 409-431.

97. J. Zheng and R. M. Dickson, *J. Am. Chem. Soc.*, 2002, **124**, 13982-13983.

98. Z. Shen, H. Duan and H. Frey, *Adv. Mater.*, 2007, **19**, 349-352.

99. F. Aldeek, M. A. H. Muhammed, G. Palui, N. Zhan and H. Mattoussi, *ACS Nano*, 2013, **7**, 2509-2521.

100. X. Huang, Y. Luo, Z. Li, B. Li, H. Zhang, L. Li, I. Majeed, P. Zou and B. Tan, *J. Phys. Chem. C*, 2011, **115**, 16753-15763.

101. Z. Li, B. Tan, M. Allix, A. I. Cooper and M. J. Rosseinsky, *Small*, 2008, **4**, 231-239.

102. Z. Li, P. W. Yi, Q. Sun, H. Lei, H. L. Zhao, Z. H. Zhu, S. C. Smith, M. Lan and G. M. Lu, *Adv. Funct. Mater.*, 2012, **22**, 2387-2393.

103. Z. Li, S. X. Wang, Q. Sun, H. L. Zhao, H. Lei, M. Lan, Z. X. Chen, X. L. Wang, S. X. Dou and G. M. Lu, *Adv. Healthcare Mater.*, 2013, **2**, 958-964.

104. M. I. Majeed, Q. W. Lu, W. Yan, Z. Li, I. Hussain, M. N. Tahir, W. Tremel and B. Tan, *J. Mater. Chem. B*, 2013, **1**, 2874-2884.

105. H. Zhang, X. Huang, L. Li, G. W. Zhang, I. Hussain, Z. Li and B. Tan, *Chem. Comm.*, 2012, **48**, 567-569.

106. L. Shang and S. Dong, *Chem. Commun.*, 2008, 1088-1090.

107. L. Li, Z. Li, H. Zhang, S. C. Zhang, I. Majeed and B. Tan, *Nanoscale*, 2013, **5**, 1986-1992.

108. R. C. Jin, *Nanoscale*, 2010, **2**, 343-362.

109. Z. Luo, X. Yuan, Y. Yu, Q. Zhang, D. T. Leong, J. Y. Lee and J. Xie, *J. Am. Chem. Soc.*, 2012, **134**, 16662-166670.

110. J. T. Petty, J. Zheng, N. V. Hud and R. M. Dickson, *J. Am. Chem. Soc.*, 2004, **126**, 5207-5212.

111. C. I. Richards, S. Choi, J. C. Hsiang, Y. Antoku, T. Vosch, A. Bongiorno, Y. L. Tzeng and R. M. Dickson, *J. Am. Chem. Soc.*, 2008, **130**, 5038-+.

112. J. P. Xie, Y. G. Zheng and J. Y. Ying, *J. Am. Chem. Soc.*, 2009, **131**, 888-889.

113. C.-L. Liu, H.-T. Wu, Y.-H. Hsiao, C.-W. Lai, C.-W. Shih, Y.-K. Peng, K.-C. Tang, H.-W. Chang, Y.-C. Chien, J.-K. Hsiao, J.-T. Cheng and P.-T. Chou, *Angew. Chem. Int. Ed.*, 2011, **50**, 7056-7060.

114. J. L. Wang, G. Zhang, Q. W. Li, H. Jiang, C. Y. Liu, C. Amatore and X. M. Wang, *Sci. Rep.*, 2013, **3**, 1157.

115. M. A. H. Muhammed, S. Ramesh, S. S. Sinha, S. K. Pal and T. Pradeep, *Nano Res.*, 2008, **1**, 333-340.

116. T. U. B. Rao and T. Pradeep, *Angew. Chem. Int. Ed.*, 2010, **49**, 3925-3929.

117. T. Udayabhaskararao, Y. Sun, N. Goswami, K. B. Samir K. Pal and T. Pradeep, *Angew. Chem. Int. Ed.*, 2012, **51**, 2155-2159.

118. H. W. Duan and S. M. Nie, *J. Am. Chem. Soc.*, 2007, **129**, 2412-2413.

119. C. A. J. Lin, T. Y. Yang, C. H. Lee, S. H. Huang, R. A. Sperling, M. Zanella, J. K. Li, J. L. Shen, H. H. Wang, H. I. Yeh, W. J. Parak and W. H. Chang, *ACS Nano*, 2009, **3**, 395-401.

120. X. Yuan, Z. Luo, Q. Zhang, X. Zhang, Y. Zheng, J. Y. Lee and J. Xie, *ACS Nano*, 2011, **5**, 8800-8808.

121. H. Xu and K. S. Suslick, *ACS Nano*, 2010, **4**, 3209-3214.

122. L. Shang, L. Yang, F. Stockmar, R. Popescu, V. Trouillet, M. Bruns, D. Gerthsen and G. U. Nienhaus, *Nanoscale*, 2012, **4**, 4155-4160.

123. Z. Wu and R. Jin, *Nano Lett*, 2010, **10**, 2568-2573.

124. H. Tsunoyama, Y. Negishi and T. Tsukuda, *J. Am. Chem. Soc.*, 2006, **128**, 6036-6037.

125. Y. Negishi, K. Nobusada and T. Tsukuda, *J. Am. Chem. Soc.*, 2005, **127**, 5261-5270.

126. C. E. Briant, B. R. C. Theobald, J. W. White, L. K. Bell, D. M. P. Mingos and A. J. Welch, *Chem. Commun.*, 1981, 201-202.

127. P. D. Jadzinsky, G. Calero, C. J. Ackerson, D. A. Bushnell and R. D. Kornberg, *Science*, 2007, **318**, 430-433.

128. M. W. Heaven, A. Dass, P. S. White, K. M. Holt and R. W. Murray, *J. Am. Chem. Soc.*, 2008, **130**, 3754-3755.

129. H. Xiang, S.-H. Wei and X. Gong, *J. Am. Chem. Soc.*, 2010, **132**, 7355-7360.

130. O. M. Bakr, V. Amendola, C. M. Aikens, W. Wenseleers, R. Li, L. D. Negro, G. C. Schatz and F. Stellacci, *Angew. Chem. Int. Ed.*, 2009, **48**, 5921-5926.

131. M. Zhu, C. M. Aikens, F. J. Hollander, G. C. Schatz and R. Jin, *J. Am. Chem. Soc.*, 2008, **130**, 5883-5885.

132. S. Link, A. Beeby, S. FitzGerald, M. A. El-Sayed, T. G. Schaaff and R. L. Whetten, *J. Phys. Chem. B*, 2002, **106**, 3410-3415.

133. Y. Yu, Z. Luo, D. M. Chevrier, D. T. Leong, P. Zhang, D.-e. Jiang and J. Xie, *J. Am. Chem. Soc.*, 2014, **136**, ASAP.

134. A. Samanta, B. B. Dhar and R. N. Devi, *J. Phys. Chem. C*, 2012, **106**, 1748-1754.

135. N. Makarava, A. Parfenov and I. V. Baskakov, *Biophys. J.*, 2005, **90**, 572-580.

136. A. Retnakumari, S. Setua, D. Menon, P. Ravindran, H. Muhammed, T. Pradeep, S. Nair and M. Koyakutty, *Nanotechnology*, 2010, **21**, 055103.

137. X. Wu, X. He, K. Wang, C. Xie, B. Zhou and Z. Qing, *Nanoscale*, 2010, **2**, 2244-2249.

138. C. Zhou, M. Long, Y. Qin, X. Sun and J. Zheng, *Angew. Chem. Int. Ed.*, 2011, **50**, 3168-3172.

139. J. Liu, M. Yu, C. Zhou, S. Yang, X. Ning and J. Zheng, *J. Am. Chem. Soc.*, 2013, **135**, 4978-4981.

140. J. Shen, Y. Zhu, X. Yang and C. Li, *Chem. Commun.*, 2012, **48**, 3686-3699.

141. X. Xu, R. Ray, Y. Gu, H. J. Ploehn, L. Gearheart, K. Raker and W. A. Scrivens, *J. Am. Chem. Soc.*, 2004, **126**, 12736-12737.

142. Y.-P. Sun, B. Zhou, Y. Lin, W. Wang, K. A. S. Fernando, P. Pathak, M. J. Meziani, B. A. Harruff, X. Wang, H. Wang, P. G. Luo, H. Yang, M. E. Kose, B. Chen, L. M. Veca and S.-Y. Xie, *J. Am. Chem. Soc.*, 2006, **128**, 7756-7757.

143. X. Wang, L. Cao, S.-T. Yang, F. Lu, M. J. Meziani, L. Tian, K. W. Sun, M. A. Bloodgood and Y.-P. Sun, *Angew. Chem. Int. Ed.*, 2010, **49**, 5310-5314.

144. S. K. Bhunia, A. Saha, A. R. Maity, S. C. Ray and N. R. Jana, *Sci. Rep.*, 2013, **3**, 1473.

145. S. Zhu, Q. Meng, L. Wang, J. Zhang, Y. Song, H. Jin, K. Zhang, H. Sun, H. Wang and B. Yang, *Angew. Chem. Int. Ed.*, 2013, **52**, 3953-3957.

146. Y. X. Fang, S. J. Guo, D. Li, C. Z. Zhu, W. Ren, S. J. Dong and E. K. Wang, *ACS Nano*, 2012, **6**, 400-409.

147. Q. L. Wang, X. X. Huang, Y. J. Long, X. L. Wang, H. J. Zhang, R. Zhu, L. P. Liang, P. Teng and H. Z. Zheng, *Carbon*, 2013, **59**, 192-199.

148. C. Ding, A. Zhu and Y. Tian, *Acc. Chem. Res.*, 2013, **46**, 10.1021/ar400023s.

149. S. N. Baker and G. A. Baker, *Angew. Chem. Int. Ed.*, 2010, **49**, 6727-6744.

150. L. Cao, X. Wang, M. J. Meziani, F. Lu, H. Wang, P. G. Luo, Y. Lin, B. A. Harruff, L. M. Veca, D. Murray, S.-Y. Xie and Y.-P. Sun, *J. Am. Chem. Soc.*, 2007, **129**, 11318-11319.

151. S. T. Yang, L. Cao, P. G. J. Luo, F. S. Lu, X. Wang, H. F. Wang, M. J. Meziani, Y. F. Liu, G. Qi and Y. P. Sun, *J. Am. Chem. Soc.*, 2009, **131**, 11308-11309.

152. X. L. Huang, F. Zhang, L. Zhu, K. Y. Choi, N. Guo, J. X. Guo, K. Tackett, P. Anilkumar, G. Liu, Q. M. Quan, H. S. Choi, G. Niu, Y. P. Sun, S. Lee and X. Y. Chen, *ACS Nano*, 2013, **7**, 5684-5693.

153. J. H. Shen, Y. H. Zhu, X. L. Yang and C. Z. Li, *Chem. Commun.*, 2012, **48**, 3686-3699.

154. L. L. Li, G. H. Wu, G. H. Yang, J. Peng, J. W. Zhao and J. J. Zhu, *Nanoscale*, 2013, **5**, 4015-4039.

155. S. J. Zhu, J. H. Zhang, S. J. Tang, C. Y. Qiao, L. Wang, H. Y. Wang, X. Liu, B. Li, Y. F. Li, W. L. Yu, X. F. Wang, H. C. Sun and B. Yang, *Adv. Funct. Mater.*, 2012, **22**, 4732-4740.

156. S. J. Zhu, J. H. Zhang, C. Y. Qiao, S. J. Tang, Y. F. Li, W. J. Yuan, B. Li, L. Tian, F. Liu, R. Hu, H. N. Gao, H. T. Wei, H. Zhang, H. C. Sun and B. Yang, *Chem. Commun.*, 2011, **47**, 6858-6860.

157. H. Tetsuka, R. Asahi, A. Nagoya, K. Okamoto, I. Tajima, R. Ohta and A. Okamoto, *Adv. Mater.*, 2012, **24**, 5333-5338.

158. X. Wu, F. Tian, W. X. Wang, J. Chen, M. Wu and J. X. Zhao, *J. Mater. Chem. C*, 2013, **1**, 4676-4684.

159. Y. Dong, H. Pang, H. B. Yang, C. Guo, J. Shao, Y. Chi, C. M. Li and T. Yu, *Angew. Chem. Int. Ed.*, 2013, **52**, 7800-7804.

160. Q. Xu, Q. Zhou, Z. Hua, Q. Xue, C. Zhang, X. Wang, D. Pan and M. Xiao, *ACS Nano*, 2013, **7**, 10654-10661.

161. S. J. Zhuo, M. W. Shao and S. T. Lee, *ACS Nano*, 2012, **6**, 1059-1064.

162. X. Sun, Z. Liu, K. Welsher, J. T. Robinson, A. Goodwin, S. Zaric and H. Dai, *Nano Res.*, 2008, **1**, 203-212.

163. J. Qian, D. Wang, F.-H. Cai, W. Xi, L. Peng, Z.-F. Zhu, H. He, M.-L. Hu and S. He, *Angew. Chem. Int. Ed.*, 2012, **51**, 10570-10575.

164. Q. Liu, B. D. Guo, Z. Y. Rao, B. H. Zhang and J. R. Gong, *Nano Lett.*, 2013, **13**, 2436-2441.

165. Z. Gu, L. Yan, G. Tian, S. Li, Z. Chai and Y. Zhao, *Adv. Mater.*, 2013, **25**, 3758-3779.

166. F. Wang and X. G. Liu, *Chem. Soc. Rev.*, 2009, **38**, 976-989.

167. F. Wang, D. Banerjee, Y. S. Liu, X. Y. Chen and X. G. Liu, *Analyst*, 2010, **135**, 1839-1854.

168. C. Bouzigues, T. Gacoin and A. Alexandrou, *ACS Nano*, 2011, **5**, 8488-8505.

169. G. Chen, C. Yang and P. N. Prasad, *Acc. Chem. Res.*, 2013, **46**, 1474-1486.

170. L. Cheng, C. Wang and Z. Liu, *Nanoscale*, 2013, **5**, 23-37.

171. L. D. Sun, Y. F. Wang and C. H. Yan, *Acc. Chem. Res.*, 2014, **47**, ASAP.

172. N. J. J. Johnson, W. Oakden, G. J. Stanisz, R. S. Prosser and F. C. J. M. van Veggel, *Chem. Mater.*, 2011, **23**, 3714-3722.

173. G. Chen, T. Y. Ohulchanskyy, R. Kumar, H. Agren and P. N. Prasad, *ACS Nano*, 2010, **4**, 3163-3168.

174. L. Gong, J. Yang, Y. Li, M. Ma, C. Xu, G. Ren, J. Lin and Q. Yang, *J. Mater. Sci.*, 2013, **48**, 3672-3678.

175. J. Ryu, H.-Y. Park, K. Kim, H. Kim, J. H. Yoo, M. Kang, K. Im, R. Grailhe and R. Song, *J. Phys. Chem.*, 2010, **114**, 21077-21082.

176. C.-f. Xu, M. Ma, L.-w. Yang, S.-j. Zeng and Q.-b. Yang, *J. Colloid Interface Sci.*, 2012, **368**, 49-55.

177. A. D. Ostrowski, E. M. Chan, D. J. Gargas, E. M. Katz, G. Han, P. J. Schuck, D. J. Milliron and B. E. Cohen, *ACS Nano*, 2012, **6**, 2686-2692.

178. J. Zhao, D. Jin, E. P. Schartner, Y. Lu, Y. Liu, A. V. Zvyagin, L. Zhang, J. Dawes, P. Xi, J. A. Piper, E. Goldys and T. M. Monro, *Nat. Nanotechnol.*, 2013, **8**, 729-734.

179. S. Heer, K. Kompe, H. U. Gudel and M. Haase, *Adv. Mater.*, 2004, **16**, 2102-2105.

180. W. Feng and L. Xiaogang, *J. Am. Chem. Soc.*, 2008, **130**, 5642-5643.

181. F. Wang, Y. Han, C. S. Lim, Y. H. Lu, J. Wang, J. Xu, H. Y. Chen, C. Zhang, M. H. Hong and X. G. Liu, *Nature*, 2010, **463**, 1061-1065.

182. F. Wang, R. R. Deng, J. Wang, Q. X. Wang, Y. Han, H. M. Zhu, X. Y. Chen and X. G. Liu, *Nat. Mater.*, 2011, **10**, 968-973.

183. H. Wen, H. Zhu, X. Chen, T. F. Hung, B. Wang, G. Zhu, S. F. Yu and F. Wang, *Angew. Chem. Int. Ed.*, 2013, **52**, 13419-13423.

184. J. Wang, R. R. Deng, M. A. MacDonald, B. L. Chen, J. K. Yuan, F. Wang, D. Z. Chi, T. S. A. Hor, P. Zhang, G. K. Liu, Y. Han and X. G. Liu, *Nat. Mater.*, 2013, **12**, 10.1038/nmat3804.

185. Q. Liu, W. Feng, T. Yang, T. Yi and F. Li, *Nat. Protoc.*, 2013, **8**, 2033-2044.

186. Y. Dai, H. Xiao, J. Liu, Q. Yuan, P. a. Ma, D. Yang, C. Li, Z. Cheng, Z. Hou, P. Yang and J. Lin, *J. Am. Chem. Soc.*, 2013, **135**, 18920-18929.

187. L. Q. Xiong, T. S. Yang, Y. Yang, C. J. Xu and F. Y. Li, *Biomaterials*, 2010, **31**, 7078-7085.

188. L. Cheng, K. Yang, M. W. Shao, X. H. Lu and Z. Liu, *Nanomedicine*, 2011, **6**, 1327-1340.

189. C. Liu, Z. Gao, J. Zeng, Y. Hou, F. Fang, Y. Li, R. Qiao, L. Shen, H. Lei, W. Yang and M. Gao, *ACS Nano*, 2013, **7**, 7227-7240.

190. S. Chinnathambi, S. Chen, S. Ganesan and N. Hanagata, *Adv. Healthcare Mater.*, 2014, **3**, 10-29.

191. M. L. Mastronardi, F. Maier-Flaig, D. Faulkner, E. J. Henderson, C. Kubel, U. Lemmer and G. A. Ozin, *Nano Lett*, 2012, **12**, 337-342.

192. J. Zou, R. K. Baldwin, K. A. Pettigrew and S. M. Kauzlarich, *Nano Lett.*, 2004, **4**, 1181-1186.

193. D. Neiner, H. W. Chiu and S. M. Kauzlarich, *J. Am. Chem. Soc.*, 2006, **128**, 11016-11017.

194. M. L. Mastronardi, F. Hennrich, E. J. Henderson, F. Maier-Flaig, C. Blum, J. Reichenbach, U. Lemmer, C. Kuebel, D. Wang, M. M. Kappes and G. A. Ozin, *J. Am. Chem. Soc.*, 2011, **133**, 11928-11931.

195. C. Tu, X. Ma, P. Pantazis, S. M. Kauzlarich and A. Y. Louie, *J. Am. Chem. Soc.*, 2010, **132**, 2016-2023.

196. M. P. Singh, T. M. Atkins, E. Muthuswamy, S. Kamali, C. Tu, A. Y. Louie and S. M. Kauzlarich, *ACS Nano*, 2012, **6**, 5596-5604.

197. M. Dasog, Z. Yang, S. Regli, T. M. Atkins, A. Faramus, M. P. Singh, E. Muthuswamy, S. M. Kauzlarich, R. D. Tilley and J. G. C. Veinot, *ACS Nano*, 2013, **7**, 2676-2685.

198. J. Fuzell, A. Thibert, T. M. Atkins, M. Dasog, E. Busby, J. G. C. Veinot, S. M. Kauzlarich and D. S. Larsen, *J. PHys. Chem. Lett.*, 2013, **4**, 3806-3812.

199. Z. F. Li and E. Ruckenstein, *Nano Lett.*, 2004, **4**, 1463-1467.

200. F. Erogbogbo, K.-T. Yong, I. Roy, G. Xu, P. N. Prasad and M. T. Swihart, *ACS Nano*, 2008, **2**, 873-878.

201. J. H. Warner, A. Hoshino, K. Yamamoto and R. D. Tilley, *Angew. Chem. Int. Ed.*, 2005, **44**, 4550-4554.

202. Y. He, Y. Zhong, F. Peng, X. Wei, Y. Su, Y. Lu, S. Su, W. Gu, L. Liao and S.-T. Lee, *J. Am. Chem. Soc.*, 2011, **133**, 14192-14195.

203. Y. Zhong, F. Peng, X. Wei, Y. Zhou, J. Wang, X. Jiang, Y. Su, S. Su, S.-T. Lee and Y. He, *Angew. Chem. Int. Ed.*, 2012, **51**, 8485-8489.

204. Y. Zhong, F. Peng, F. Bao, S. Wang, X. Ji, L. Yang, Y. Su, S.-T. Lee and Y. He, *J. Am. Chem. Soc.*, 2013, **135**, 8350-8356.

205. H. Sugimoto, M. Fujii, Y. Fukuda, K. Imakita and K. Akamatsu, *Nanoscale*, 2014, **6**, 122-126.

206. F. Erogbogbo, K.-T. Yong, I. Roy, R. Hu, W.-C. Law, W. Zhao, H. Ding, F. Wu, R. Kumar, M. T. Swihart and P. N. Prasad, *ACS Nano*, 2011, **5**, 413-423.

207. J. W. Liu, F. Erogbogbo, K. T. Yong, L. Ye, J. Liu, R. Hu, H. Y. Chen, Y. Z. Hu, Y. Yang, J. H. Yang, I. Roy, N. A. Karker, M. T. Swihart and P. N. Prasad, *ACS Nano*, 2013, **7**, 7303-7310.

208. C. Tu, X. Ma, A. House, S. M. Kauzlarich and A. Y. Louie, *ACS Med. Chem. Lett.*, 2011, **2**, 285-288.

209. N. Mitchell, T. L. Kalber, M. S. Cooper, K. Sunassee, S. L. Chalker, K. P. Shaw, K. L. Ordidge, A. Badar, S. M. Janes, P. J. Blower, M. F. Lythgoe, H. C. Hailes and A. B. Tabor, *Biomaterials*, 2013, **34**, 1179-1192.

210. M. Braddock, ed., *Biomedical Imaging: The Chemistry of Labels, Probes and Contrast Agents*, Royal Society of Chemistry, 2012.

211. N. Lee, H. R. Cho, M. H. Oh, S. H. Lee, K. Kim, B. H. Kim, K. Shin, T. Y. Ahn, J. W. Choi, Y. W. Kim, S. H. Choi and T. Hyeon, *J. Am. Chem. Soc.*, 2012, **134**, 10309-10312.

212. H. Y. Xing, W. B. Bu, S. J. Zhang, X. P. Zheng, M. Li, F. Chen, Q. J. He, L. P. Zhou, W. J. Peng, Y. Q. Hua and J. L. Shi, *Biomaterials*, 2012, **33**, 1079-1089.

213. J.-S. Choi, J.-H. Lee, T.-H. Shin, H.-T. Song, E. Y. Kim and J. Cheon, *J. Am. Chem. Soc.*, 2010, **132**, 11015-11017.